ISSN : 2800-1729 **Edition : Vol 5. Num 2 (2026)**

Biopolymer Applications Journal

Editor in chief:
Pr. HAMMICHE Dalila

UNIVERSITÉ ABDERRAHMANE MIRA - BEJAIA
FACULTÉ DE TECHNOLOGIE

www.univ-bejaia/baj

ISSN : 2800-1729

Table of content

Biopolymer Applications Journal ***Dalila Hammiche et al. Vol 5 N° 2, 2026, pp. 01-06***
e-ISSN: 2800-1729

General Overview of Starch as a Biodegradable film Material

Dalila Hammiche [1] ; Rebiha Bellache[1,2*] ; Samra Isadounene [1]
[1]*Universite de Bejaia, Faculté de Technologie, Laboratoire des Matériaux Polymères Avancés Route De Targa- Ouzemmour, Bejaia 0600, Algérie*
[2]*Universite M'Hamed Bougara de Boumerdès, Faculté de Technologie, Département de Génie des Procédés, Boumerdès 35000, Algérie*
**Corresponding author* *rebiha.bellache@univ-bejaia.dz*
Received: 14 June 2026; Accepted: 02 July 2026; Published: 12 July 2026

Abstract

The characteristics of starch-based films are profoundly governed by their chemical constitution, structural arrangement, and the extent of crystallinity, which are pivotal in ascertaining their functional capabilities and performance metrics. Mechanical properties constitute critical variables for assessing the appropriateness of starch films for various practical utilizations. These characteristics are contingent upon the source of starch, the conditions under which processing occurs, and the incorporation of additives such as plasticizers and reinforcement agents. An increase in crystallinity typically enhances the tensile strength and rigidity of the films, notwithstanding the potential compromise in flexibility. Barrier properties are of equal significance, especially in the context of food packaging applications. The permeability to water vapor and oxygen is markedly influenced by the microstructural attributes of starch films. Crystalline domains within the polymeric matrix are regarded as impervious to gases and moisture. Furthermore, a salient advantage of starch-derived materials is their inherent biodegradability. These films possess the capability to be decomposed by microorganisms and enzymes in appropriate environmental settings, thereby aiding in the alleviation of plastic pollution.

Keywords: *Starch, biofilm, mechanical properties, permeability*

I. Introduction

The escalating environmental issues related to the pervasive utilization of petroleum-derived plastics and the resultant accumulation of non-biodegradable waste have stimulated the pursuit of sustainable and environmentally benign alternatives. In this regard, biodegradable films originating from renewable natural resources have garnered substantial interest in recent years. Among the diverse array of biopolymers evaluated for biofilm fabrication, starch is distinguished as one of the most promising substances owing to its widespread availability, cost-effectiveness, biodegradability, and exceptional film-forming characteristics. [1]

Starch represents a naturally occurring polysaccharide that functions as the principal energy reservoir in numerous plant species, including corn, potato, wheat, rice, and cassava. It is recognized as one of the most plentiful renewable biopolymers on the planet and assumes a vital role in both human dietary intake and industrial use. Chemically, starch is composed of two predominant glucose polymers: amylose and amylopectin. Amylose is primarily a linear molecule constituted of α-(1→4)-linked glucose units, whereas amylopectin is a highly branched polymer featuring both α-(1→4) and α-(1→6) glycosidic bonds. The relative proportions of these two constituents substantially affect the physicochemical and mechanical properties of starch-based materials. [2]

A critical characteristic of starch is its capacity to form films. When starch is dispersed in aqueous solutions and subjected to heating, a phenomenon known as gelatinization transpires. During this phase, starch granules absorb water, expand, and partially relinquish their crystalline configuration, permitting polymer chains to attain greater mobility. Upon cooling and desiccation, these chains engage in hydrogen bonding interactions, culminating in the establishment of a continuous and cohesive film matrix (**Figure 1**). This film-forming ability has prompted extensive exploration of starch as a biodegradable substitute for traditional synthetic plastics. [3]

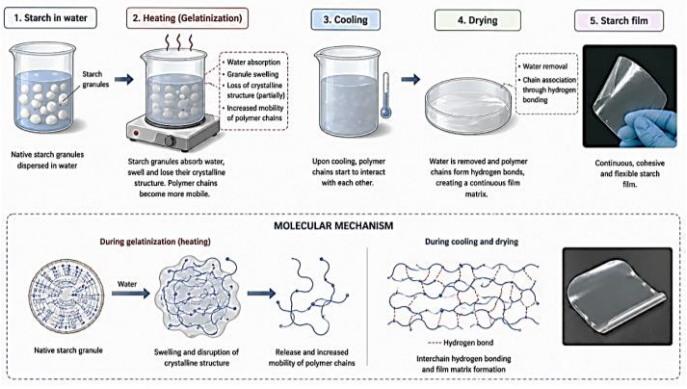

Figure 1: starch biofilm formation process

Starch-based biofilms present numerous advantages. They are derived from renewable agricultural resources, are typically non-toxic, and can be entirely degraded by microorganisms under suitable environmental conditions. These attributes render them eco-friendly materials capable of mitigating plastic pollution and reducing reliance on fossil fuel resources. Moreover, starch films display favourable characteristics such as good transparency, odourless properties, and relatively low oxygen permeability, which are particularly advantageous in food packaging applications. [4]

Notwithstanding these benefits, starch-based biofilms also exhibit certain constraints. The hydrophilic nature of starch molecules renders these films highly susceptible to moisture and water absorption. Exposure to humid conditions may result in swelling, diminished mechanical integrity, and inadequate barrier properties against water vapor. Additionally, films generated from pure starch frequently exhibit brittleness and lack the requisite flexibility for practical applications. To address these limitations, plasticizers such as glycerol, sorbitol, and polyethylene glycol are routinely incorporated into starch formulations. These additives enhance film flexibility by diminishing intermolecular interactions among polymer chains. [5]

Recent investigations have concentrated on augmenting the performance of starch-based biofilms through blending and composite formation. A variety of natural polymers, including gelatin, chitosan, cellulose derivatives, and plant proteins, have been amalgamated with starch to enhance mechanical, thermal, and barrier properties. Furthermore, the inclusion of nanoparticles, nanocellulose, essential oils, and plant extracts has been assessed to impart antimicrobial, antioxidant, and functional attributes. These modifications have considerably broadened the prospective applications of starch-based films in food packaging, agriculture, pharmaceutical products, and biomedical domains.[6]
In the domain of food packaging, starch-derived biofilms have garnered notable attention as sustainable alternatives to traditional packaging materials. They may serve as either independent packaging films or as edible coatings that are directly applied to the surfaces of food products. Such implementations contribute to the preservation of food quality, the mitigation of moisture loss, the restriction of microbial proliferation, and the prolongation of shelf life, all while reducing ecological footprints. Furthermore, the increasing consumer inclination towards biodegradable and environmentally-friendly products has significantly propelled research and innovation in this field. [7]
In summation, starch is recognized as one of the most promising natural polymers for the synthesis of biodegradable biofilms. Its extensive availability, renewability, economic feasibility, and superior film-forming capabilities render it an appealing candidate for the development of sustainable materials. Despite the persistence of challenges pertaining to moisture susceptibility and mechanical performance, ongoing advancements in starch modification techniques and composite material technology are progressively enhancing the functionality and versatility of starch-based biofilms. Consequently, it is anticipated that starch will assume a crucial role in the forthcoming advancement of eco-friendly packaging solutions and biodegradable materials. In this review, mechanical properties, permeability and biodegradation of starch will be underscored.

II. Mechanical properties

The possession of favourable mechanical properties is imperative for the practical utilization of food packaging materials [8]
Nevertheless, in comparison to analogous applications of conventional plastics, starch-based biodegradable packaging manifests significant shortcomings attributable to its inferior mechanical properties [9] thereby constraining its applicability in food and product packaging [10] Superior mechanical properties can be harnessed to substantial advantage in traditional packaging contexts. Consequently, it is crucial to enhance the mechanical properties of starch-based films.
Blending approaches have been shown to significantly enhance the mechanical properties of starch-based films, making them more suitable for various applications. This improvement is often achieved by combining starch with other materials and plasticizers.

Starch, when blended with lime and citrus pectin, can form strong, self-supporting films. Researchers have investigated the use of different plasticizers, such as glycerin, urea, and polyethylene glycol, in these blends to characterize their ability to form such films. Among the plasticizers studied, glycerin demonstrated the best results, leading to films with strong, high modulus [11].
Numerous endeavors have been undertaken to formulate PLA/starch composites with the objective of minimizing the overall expenditure of raw materials while simultaneously augmenting their biodegradability. A predominant challenge associated with this composite system is the inadequate interfacial synergy between the

hydrophilic starch granules and the hydrophobic PLA. The mechanical characteristics of PLA and starch blends produced through traditional methodologies exhibit significant deficiencies due to the inherent incompatibility [12]. Polycaprolactone (PCL) represents an additional class of biodegradable polymer. The literature has extensively documented the interactions between starch and PCL blends. The limitations inherent in pure starch materials, such as diminished resilience, heightened moisture sensitivity, and pronounced shrinkage, have been effectively mitigated by the incorporation of PCL into the starch matrix, even at minimal concentrations of PCL. The blending process with PCL markedly enhances the impact resistance of the composite [13].

In summary, blending starch with various components like lime, citrus pectin, and different plasticizers, particularly glycerin, is a proven method to enhance the mechanical strength and modulus of starch-based films. This approach also contributes to improving biodegradability and other functional properties, expanding the potential applications of starch in sustainable materials.

III. Permeability

Starch permeability represents a significant characteristic that governs the capacity of water, gases, or other entities to traverse starch-derived materials. It serves a vital function in domains such as food packaging, biodegradable films, and pharmaceutical applications. The permeability of starch is influenced by various factors including its chemical composition, molecular architecture, and ambient environmental conditions. A comprehensive understanding and regulation of starch permeability may enhance the efficacy and sustainability of materials derived from starch.

It was noticed that Starch biofilms extracted from melloco and mashua exhibited higher water vapor permeability (WVP) compared to those from oca and potato, attributed to stronger starch-starch interactions in the latter, indicating varying moisture interactions based on the starch source [12].

The incorporation of glycerol, which engages in interactions with starch macromolecules, into the starch-based film results in an augmentation of the free volume within the film matrix. This modification facilitates an enhancement in molecular mobility, thereby rendering hydroxyl moieties more amenable to hydrogen bonding interactions with water molecules. The substitution of phenolic compounds with glycerol subsequently diminishes the affinity for water in the films, attributed to an intermolecular interaction between glycerol and the hydroxyl groups present in the starch chains [13]. As per a certain study, the integration of citric acid within potato starch-based films resulted in an enhancement of water vapor permeability [14,15].

According to Ramesh et al [16], Water-vapor permeability of starch-based biofilms, specifically avocado seed starch, decreases with increased concentrations of Tween-20 and sorbitol, while higher starch and agar concentrations increase WP due to enhanced intermolecular connections and free space within the film matrix.

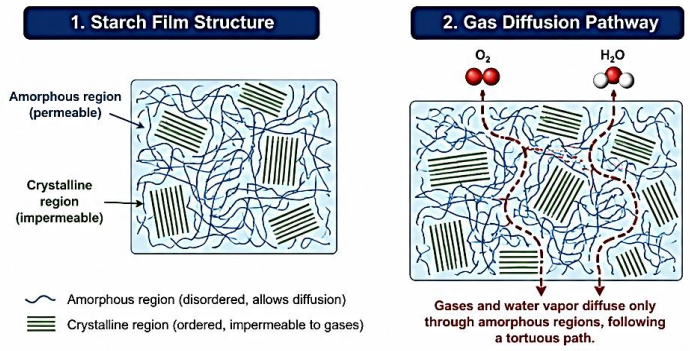

Figure 2: Effect of crystallinity on the permeability of starch-based films

Oxygen infiltration is a critical factor in food spoilage, as it facilitates the growth of aerobic microorganisms and leads to chemical deterioration. To mitigate this, starch-based materials are often enhanced with fillers or nanoparticles to create high-barrier composites. Adding 5% nitrite to a blend of polybutylene diacrylate (PBAT) and thermoplastic starch (TPS) modifies chemical bonds and microstructures, resulting in oxygen permeability comparable to fossil-based plastics. Nanoclay Reinforcement: Nanoclay combined with starch-polyacrylic acid through in-situ polymerization significantly fortifies oxygen resistance. Starch/PVA/Clay Nanocomposites: Using 50% Polyvinyl alcohol (PVA) in a starch/clay nanocomposite can reduce oxygen permeability by approximately 210% through a continuous phase change mechanism. Gas transmission rates are known to decrease as amylose content increases. This is demonstrated by comparing starch sources: potato peel starch, which is richer in amylose (~31%), produces films with a much lower oxygen permeability (0.285 Barrer) compared to starch from the potato itself (0.698 Barrer). Additionally, crystalline zones within the film are considered impermeable to gases. Therefore, starch sources that favour higher crystallinity like those derived from potato waste, naturally provide better protection (Figure 2). Moreover, the addition of plasticizers like glycerol creates a strong interconnecting polymer network that influences the free

volume of the matrix, which can further decrease oxygen permeation. [17-19]

IV. Environmental impacts

Starch-based materials reduce reliance on fossil polymers and can be compostable when correctly formulated, which is attractive for regions with limited recycling infrastructure. However, life-cycle impacts vary by formulation, processing route, and end-of-life management, so outcomes are context dependent. Table 1 encapsulates the ecological, resource-utilization, and post-consumer disposal dimensions of starch-derived biodegradable packaging.

Table 1: Sustainability Advantages and Obstacles of Starch-Derived Biodegradable Packaging

Aspect	Key benefits	Main concerns	Evidence
Environmental	Reduced fossil polymer use and potential for compostability	Performance-driven losses (e.g., moisture ingress) and variable LCA outcomes depending on processing and end-of-life	Starch suitability for biodegradable packages and compostable alternatives is reported [20, 21]
Resource use	Uses widely available plant starch as feedstock	Feedstock sourcing and processing energy can change impacts	Availability and low-tech production noted for developing contexts [20, 22]
End of life	Can lower plastic litter if composted or collected separately	Benefits require appropriate collection/composting infrastructure; otherwise, gains are limited	Importance of local waste systems and recycling to reduce impacts demonstrated in regional LCA work [20, 21]

It underscores significant advantages such as diminished dependence on petroleum-based plastics, renewable starch feedstocks, and potential for compostability, while concurrently delineating issues associated with performance, the implications of feedstock processing, and the necessity for robust waste management systems. The evidence column cites empirical studies that corroborate these benefits and drawbacks.

V. Conclusions

Starch-based packaging can provide low-cost, locally sourced biodegradable alternatives to single-use plastics but environmental benefits depend on formulation, barrier performance, and waste infrastructure. Industrial scaling faces technical, economic, and food-security trade-offs that require targeted investment and standards.

Starch-derived films have emerged as viable alternatives to traditional petroleum-derived plastics owing to their renewability, biodegradability, and environmental sustainability. The overall efficacy of these films is dictated by several critical factors, including mechanical properties, permeability to water vapor and oxygen, and biodegradation characteristics. These attributes are significantly impacted by the source of the starch, its molecular composition, the conditions under which it is processed, and the degree of crystallinity attained. An increase in crystallinity typically enhances barrier properties by diminishing gas and moisture permeability, while the interplay between crystalline and amorphous domains influences both mechanical strength and the rate of degradation.

Additionally, the incorporation of plasticizers, fillers, or reinforcing agents can markedly enhance the performance of the films and expand their applicability. Consequently, the optimization of the structural and compositional aspects of starch-based materials is imperative for the development of sustainable packaging solutions that integrate sufficient mechanical strength, effective barrier characteristics, and controlled biodegradability.

References:

1. S. Kamalakkannan, A. Abeynayaka, A. K. Kulatunga, R. Singh, M. Tatsuno, P. J. D. Gamaralalage. Life Cycle Assessment of Selected Single-Use Plastic Products towards Evidence-Based Policy Recommendations in Sri Lanka. Sustainability. 14(21), 14170, 2022. https://doi.org/10.3390/su142114170

2. k. Anand, S. Saranyadevi, T. K. Selva, N. Shankar, V. P. Subhash, S. Liu, A. Sadaqat, S. Wei. Starch based

biodegradable packaging systems and their interactions with food components, shelf-life implications: A review, Carbohydrate Polymer Technologies and Applications, 13, 101067, 2026 https://doi.org/10.1016/j.carpta.2025.101067

3. S. Weng, I. Marcet, M. Rendueles, M. Díaz. Edible films from the laboratory to industry: A review of the different production methods. Food and Bioprocess Technology, 18 (4) 3245-3271, 2025. https://doi.org/10.1007/s11947-024-03641-4

4. A. Karnwal, A. Rauf, A.Y. Jassim, M. Selvaraj, A.R.M. S. Al-Tawaha, P. Kashyap, D. Kumar, T. Malik. Advanced starch-based films for food packaging: Innovations in sustainability and functional properties. Food Chemistry: X, 29, 102662, 2025. https://doi.org/10.1016/j.fochx.2025.102662

5. G.K. Malik, A. Khuntia, J. Mitra. Comparative Effect of Different Plasticizers on Barrier, Mechanical, Optical, and Sorption Properties of Hydroxypropyl Methylcellulose (HPMC)–Based Edible Film. Journal of Biosystems Engineering, 47 (2), 2022, 93-105, https://doi.org/10.1007/s42853-022-00132-2

6. A. Bapan, B. Soubani, T. Yoshikuni. Biopolymers and their nanocomposites coated paper-based high barrier and sustainable food packaging materials. Carbohydrate Polymers. 367, 123966, 2025. https://doi.org/10.1016/j.carbpol.2025.123966

7. A. Matloob, A. Hudda, M. Mohsein, S. Ambreen, F. Atta Khan, S. Oranab, M. A. Rahim, W. Khalid, G. Ahmad, N. Seema, R. S. Ercisli. A Review on Edible Coatings and Films: Advances, Composition, Production Methods, and Safety Concerns. ACS Omega. 8, 32, 28932–28944, 2023. http://pubs.acs.org/journal/acsodf?ref=pdf

8. M.K. Lauer, R.C. Smith. Recent advances in starch-based films toward food packaging applications: Physicochemical, mechanical, and functional properties. Comprehensive Reviews in Food Science and Food Safety. 19, 3031–3083, 2020. https://doi.org/10.1111/1541-4337.12627

9. B. Khan, M.B.K. Niazi, G. Samin, Z. Jahan. Thermoplastic Starch: A Possible Biodegradable Food Packaging Material-A Review. Journal of Food Process Engineering. 40, e12447, 2017. https://doi.org/10.1111/jfpe.12447

10. C. Congli, J. Na, W. Yanfei, X. Liu, S. Qingjie. Bioactive and intelligent starch-based films: A review. Trends Food Science and Technology. 116, 854–869, 2021. https://doi.org/10.1016/j.tifs.2021.08.024

11. S. Pokhrel. A review on introduction and applications of starch and its biodegradable polymers. International Journal of Environment, 4(4), 114-125, 2015. https://doi.org/10.3126/IJE.V4I4.14108

12. N. Wang, J. G. Yu, P. R. Chang, X. Ma: Influence of formamide and water on the properties of thermoplastic starch/poly (lactic acid) blends. Carbohydrate Polymers, 71, 109118 (2008). https://doi.org/10.1016/j.carbpol.2007.05.025

13. R. P. Singh, J. K. Pandey, D. Rutot, Ph. Degée, Ph. Dubois: Biodegradation of poly(ε-caprolactone)/ starch blends and composites in composting and culture environments: The effect of compatibilization on the inherent biodegradability of the host polymer. Carbohydrate Research, **338**, 1759–1769 (2003). https://doi.org/10.1016/S0008-6215(03)00236-2

14. C. Pico, J. De la Vega, I. Tubon, M. Arancibia, S. Casado. Nanoscopic Characterization of Starch Biofilms Extracted from the Andean Tubers Ullucus tuberosus, Tropaeolum tuberosum, Oxalis tuberosa, and Solanum tuberosum. Polymers, 14(19), 4116, 2022. https://doi.org/10.3390/polym14194116

15. C. Menzel, C. González-Martínez, F. Vilaplana, G. Diretto, A. Chiralt. Incorporation of natural antioxidants from rice straw into renewable starch films. International Journal of Biological Macromolecules. 146, 976-986, 2020. https://doi.org/10.1016/j.ijbiomac.2019.09.222

16. E. Olsson, C. Menzel, C. Johansson, R. Andersson, K. Koch, L. Järnström. The effect of pH on hydrolysis, cross-linking and barrier properties of starch barriers containing citric acid. Carbohydrate Polymer, 98, 1505-1513, 2013. https://doi.org/10.1016/j.carbpol.2013.07.040

17. L. Stoll, A.M.D. Silva, A.O.E.S. Iahnke, T.M.H. Costa, S.H. Flores, A.D.O. Rios. Active biodegradable film with encapsulated anthocyanins: Effect on the quality attributes of extra-virgin olive oil during storage. J. Food Process. Preserv. 41, e13218, 2017. https://doi.org/10.1111/jfpp.13218

18. R. Ramesh, H. Palanivel, S. V. Prabhu, B. Z. Tizazu, A. A. Woldesemayat. Process Development for Edible Film

Preparation Using Avocado Seed Starch: Response Surface Modeling and Analysis for Water-Vapor Permeability. Advances in Materials Science and Engineering, Volume 2023, Article ID 9895647, 1-7, 2021. https://doi.org/10.1155/2021/7859658

19. K. Wattinee, W. Phanwipa, , K. Phatthranit, H. Nathdanai. Thermoplastic starch blown films functionalized by plasticized nitrite blended with PBAT for superior oxygen barrier and active biodegradable meat packaging. Food Chemistry 374, 131709, 2022. https://doi.org/10.1016/j.foodchem.2021.131709

20. P.K. Sethy, K. Prusty, P. Mohapatra, S.K. Swain. Nanoclay decorated polyacrylic acid/starch hybrid nanocomposite thin films as packaging materials. Polymer Composites. 40, 229-239, 2019. https://doi.org/10.1002/pc.24636

21. W. Wang, H. Zhang, R. Jia, Y. Dai, H. Dong, H. Hou, Q. Guo. High performance extrusion blown starch/polyvinyl alcohol/clay nanocomposite films. Food Hydrocolloids. 79, 534-543, 2018. https://doi.org/10.1016/j.foodhyd.2017.12.013

Biopolymer Applications Journal
e-ISSN: 2800-1729
Mokhtar BENCHERIF et al. Vol 5 N° 2, 2026, pp. 07-15

DNLR Approach of the Behavior and Damage of Thermoplastic Polymers (HDPE)

Mokhtar BENCHERIF[1*] ; Amar BOUDEDJA [1] ; Rabah FERHOUM [1] ; Madjid ALMANSBA [1]
1: Laboratory of Materials Elaboration, Characterization and Modeling (LEC2M), Faculty of Construction Engineering, Mouloud Mammeri University Tizi Ouzou, 15000 Tizi Ouzou, DZ.
**Corresponding author email: mokhtar.bencherif@ummto.dz*
Received: 13 June 2026; Accepted: 29 June 2026; Published: 13 July 2026

Abstract

This study proposes a novel formulation of the Distribution of Non-Linear Relaxation (DNLR) model to accurately capture the mechanical behavior and damage evolution of semi-crystalline thermoplastic polymers, specifically high-density polyethylene (HDPE), under large uniaxial deformations. Building upon the generalized Gibbs relationship for out-of-equilibrium systems, the proposed approach integrates an effective elastic modulus to account for damage-induced stiffness degradation. The model uses an empirical constitutive law to describe the evolution of the Young's modulus as a function of axial strain, coupled with a statistical hyperelastic framework to define the equilibrium stress response. Numerical simulations reveal that the apparent elastic modulus initially decreases significantly due to micro-cavitation damage, followed by a continuous recovery phase driven by macromolecular chain reorientation until ultimate failure. The predicted stress-strain curves and modulus evolution demonstrate strong agreement with experimental tensile data across the entire deformation range. These findings confirm that the enhanced DNLR formulation effectively bridges dissipative thermodynamics with microscopic deformation mechanisms, providing a robust predictive tool for modeling damage progression and non-linear viscoelastic behavior in thermoplastic and biopolymer systems. The model's capacity to quantitatively reproduce high-deformation experimental responses highlights its potential for advanced material characterization and structural integrity assessment.

Keywords: *Constitutive modeling, Damage evolution, High-density polyethylene, Irreversible thermodynamics, Non-linear relaxation.*

I. Introduction

The plastic deformation mechanisms in semi-crystalline High-Density Polyethylene (HDPE[1]) are governed by complex interactions between its amorphous and crystalline phases [1], [2]. At small deformations, interlamellar sliding and the rotation of crystalline stacks predominate, while increased stress activates primary crystallographic mechanisms such as chain-direction and perpendicular slip, occasionally accompanied by twinning or martensitic transformations [1], [3]. As deformation progresses, the original lamellar structure undergoes fragmentation and micronecking, reorganizing into a fibrillar structure interconnected by highly stretched tie molecules, which induces hyperelastic hardening [1], [2], [3]. Concurrently, this structural evolution is intrinsically linked to damage mechanisms, notably cavitation and microvoid formation near the yield point, which accelerate lamellar fragmentation as the material approaches failure [1].

HDPE is a semi-crystalline polymer, its crystallization result from the regular piling of macromolecular chains. Their extremities are different from the rest of the polymer, these macromolecules cannot be fully regular. As a result, the existence of both amorphous and crystalline phases [1]. This microstructure is described at first by the fringe and micelles model [4], in which the crystalline zones are represented by ordered sequences where the chains are aligned. The size of the crystalline zones varies between 5 and 50 nm. In considering their length, the macromolecules can be parts of many crystals, which are guided at random. We can distinguish two extreme configurations related to the folding of macromolecular chains: tight arrangement and disordered arrangement [3], [4]. In this last case, the same chain can then participate at the same time to the amorphous and the crystalline phases [5] contrary to the first mode of folding where the chain participates only to the crystallite formation [4].

One of the most remarkable characteristics of semi-crystalline thermoplastics is their capacity to undergo a large plastic deformation before the break at room temperature [1], [4]. This phenomenon results partially because their glassy

[1] HDPE : High Density Polyethylene

transition temperature (-100°C for PE[2]) is well situated below the ambient temperature [1], [6]. Contrary to the glassy polymers for which the deformation is located in the fine bands of cutting, for the semi-crystalline polymers the plastic deformation intervenes in a macroscopic and not homogeneous way in tests of uniaxial drive [7], [8]. This phenomenon of deformation localization, called striction or plastic instability, was widely studied [1], [3], [5], [9].

To describe an efficient behaviour law for this material, we recourse to a model using the approach developed by Cunat [10], [11], based on the Thermodynamics of the Irreversible Processes (TPI) to the scale of the RVE[3] [1], [6]. This approach leans on Gibbs relationship generalization in the case where the local equilibrium balance is broken [6], [11], [12]. It defines itself like an extension of the concepts initially introduced by De Donder [11], [13], [14], the local dissipation can be considered physically as the result of definite internal reorganizations assimilated to non-stochiometric chemical reactions; these processes are characterized then by their degrees of advancement and their affinities [1], [6]. The idea is to achieve a modal description in presence of non-linearities [11], [15]. This approach was used with success these last years, to simulate elastic-viscoplastic polymers' behaviour. The beginning works were especially focused on the definition and on the role of the relaxed state and the spectre of the time relaxation in the modelling. Several writings were proposed, we shall evoke only that of Loukil, M'rabet and Arieby concerning the mechanical behaviour modelling of the semi-crystalline polymers, particularly HDPE.

In the present work, we remind firstly the theoretical framework and the rheological model, which is adopted and secondly, we suggest a new formulation of the D.N.L.R[4]. model, which considers the damaging effects.

II. Material and methods

II.1 Material Specification and Specimen Characteristics

The material investigated in this study consists of high-density polyethylene (HDPE), specifically PE100 grade granules supplied by the CHIALI company (Sidi Bel Abbes, Algeria) [16]. This semi-crystalline thermoplastic is characterized by a molar mass of approximately 300,000 g/mol and exhibits a structural morphology composed of spherulitic aggregations of amorphous and crystalline phases. Differential scanning calorimetry (DSC) characterization established the melting temperature (T_m) at 135°C and the glass transition temperature (T_g) at -125°C [16].

II.2 Uniaxial Tensile Testing Configuration

Mechanical characterization was performed using a universal servo hydraulic tensile testing apparatus (MTS systems) under strict isothermal conditions at 25°C [15], [16]. To accurately capture the material's true stress-strain response and damage progression, all tests were conducted under local strain-rate control at a constant rate of $\dot{\varepsilon} = 10^{-3}s^{-1}$.

The local deformations within a Representative Volume Element (RVE) were monitored in real-time using the VideoTraction system [8], [15]. This intelligent optical extensometer utilizes a digital camera to analyze the relative displacements of dot markers printed on the specimen surface [8], [15]. This technique enables the real-time calculation of true (rational) axial strain and true stress, the latter accounting for the instantaneous reduction in cross-sectional area during drawing and localized necking [8], [15]. The experimental data thus obtained, specifically the Young's modulus, yield stress, and hardening behavior, served as the primary calibration set for identifying the numerical parameters of the proposed DNLR model.

III. Theoretical package

III.1 The D.N.L.R. approach and Constitutive equations

The DNLR approach has been initially proposed by Cunat in 1988 [9] for simulating the behaviour of liquid during a decreasing temperature. It is based on a statistical mechanics considering that each "particle" of the material has its own dynamics for its motion degree of freedom (vibration, translation or even rotation). The word ''particle'' means elementary particle (atomic size) or group of particles (cluster), which can be treated with a specific dynamics. The evolution of the corresponding population results from the equilibrium condition by assuming that there is no excess term for the mixing of several particles. Hence, it is possible to build the macroscopic response and to obtain the specific heat as well as the enthalpy or the entropy. This corresponds to the equilibrium or relaxed state. In the case of a sudden quench of a liquid, Cunat assumes that it appears as an excess term of energy or entropy associated with an activity coefficient for each particle. This term plays the role of the composition adaptation in order to establish a partial equilibrium or a constrained equilibrium. The obtained deviation from the equilibrium is just the fluctuation used in the DNLR theory. Due to practical reasons, the specificity of the DNLR is to choose a modal base. The principal advantage of this approach is based on

[2] PE : Polyethylene
[3] RVE : Representative Volume Element
[4] D.N.L.R : Distribution of Non-Linear Relaxations

the introduction of a quasi-infinite number of dissipative modes using only two adjustable parameters for describing the corresponding relaxation spectrum by means of fluctuation theory.

The developed constitutive laws aim to describe the mechanical behaviour of material based on two principle foundations expressed in a representative volume element (RVE):

1. The first one consists to admit that even in out-of-equilibrium condition, the internal energy remains as an extensive quantity and keeps the status of a potential controlled by three independent extensive variables: (i) the entropy (thermal part of the energy), (ii) the volume variations caused by deformation (mechanical part of the energy) and (iii) the whole number of species forming the volume subjected to internal reactions (chemical part of the energy). The potential is a function of two kinds of state variables: internal and observable ones.
2. The second foundation is based on the use of the fluctuation theory to statistically describe the dissipative phenomena in the material.

For each element in a given system, a set of degrees of freedom or internal variables can be used to describe the actual configuration and its dynamic evolution traducing the internal reorganizations. In equilibrium state, these variables are no longer independent and become functions of the controlled variables directly depending on the boundary conditions.

The idea which prevails to the D.N.L.R. formalism consists to spread the common concepts of thermodynamics to situations of non-equilibrium. We admit that the generalized Gibbs relation maintains its status related to a potential function and it contains all the information. It expresses notably the equivalence of the three forms which are related to internal energies, say thermal, mechanical and chemical.

The starting point is the writing of the internal energy as a potential of Gibbs.

$$U = Ts + \sigma e + \sum_k \mu_k \eta_k \ , \qquad (1)$$

where s, e and η_k represent respectively, the specific entropy, the strain vector and the mole number of components $k. T, \sigma$ and μ_k are their associated dual variables representing, respectively, the temperature, the stress vector and the chemical potential.

The different terms in Eq. (1) are defined as the first order partial derivatives of internal energy. At the equilibrium state, they recover their usual signification, i.e., the thermometric value of the temperature for example.

For a regular representative volume element (RVE), the internal energy is expressed according to variables of a thermal and mechanical origin and internal variables of a microstructure origin. We can, then write the Gibbs relation in a more condensed form:

$$\dot{U} = Y \cdot \dot{y} \qquad (2)$$

With $Y = \frac{\partial U}{\partial y} = (T, \sigma, A)$ which represents the generalized force to $y = (s, e, z)$, the vector of extensive variables. The affinity A is the thermodynamic force which is associated to the independent and internal variables z. The principal variation which prevails to the second law of the thermodynamics induces naturally the return of the system in its equilibrium state.

To characterize the local behaviour of the elementary representative volume, we consider the new potential $\Psi = \Psi(\gamma, z)$, where γ and z are, respectively, the vectors of controlled and internal variables. Indeed, the form of the potential is not unique, and the use of the Legendre rules allows modifying the potential with respect to the observable variables at the RVE boundaries. The variation of this potential is adapted to experimental conditions and is written as:

$$d\psi_k = \sum_{m=1}^{q} \beta_m d\gamma_m - \sum_{j=1}^{p} A^j dz^j \ , \qquad (3)$$

where q and p are the dimensions of generalized size γ and z respectively.

The variables β_m and γ_m represent respectively the observable variables and the perturbation of the system. In case of an elastic-plastic behaviour, β corresponds to a stress σ and γ to a strain ε.

After differentiation of eq. (3), one obtains

$$\beta_m\left(\gamma_n, z^j\right) = \frac{\partial \psi_k\left(\gamma_n, z^j\right)}{\partial \gamma_m} \qquad (4)$$

$$A^j\left(\gamma_m, z^j\right) = \frac{\partial \psi_k\left(\gamma_n, z^j\right)}{\partial z^j} \qquad (5)$$

Then:

$$d\beta_m\left(\gamma_n, z^j\right) = \sum_{n=1}^{q} \frac{\partial^2 \psi_k\left(\gamma_n, z^j\right)}{\partial \gamma_m \partial \gamma_n} d\gamma_n + \sum_{j=1}^{p} \frac{\partial^2 \psi_k\left(\gamma_n, z^j\right)}{\partial \gamma_m \partial z^j} dz^j \qquad (6)$$

$$dA^j\left(\gamma_m, z^j\right) = -\sum_{n=1}^{q} \frac{\partial^2 \psi_k\left(\gamma_n, z^j\right)}{\partial z^j \partial \gamma_n} d\gamma_n - \sum_{j=1}^{p} \frac{\partial^2 \psi_k\left(\gamma_m, z^j\right)}{\partial \gamma z^j \partial z^j} dz^j \qquad (7)$$

From which the writing, under the following matrix form:

$$\dot{\sigma} = a^u.\dot{\varepsilon} + \bar{b}.\dot{z} \quad (8)$$

$$-\dot{A} = \bar{b}^t.\dot{\varepsilon} + g.\dot{z}\,, \quad (9)$$

where a^u is a square symmetric tensor of Tisza which is responsible for the instantaneous response of the system and coupling the controlled state variables with themselves. The matrix $\bar{b}$ is a rectangular tensor coupling the reversible state variables with the irreversible ones to describe the dissipation. g is a definite positive square symmetric tensor coupling the internal variables with themselves.

The two constitutive and incremental relations (8) and (9) can be written in a synthetic manner as follows:

$$\begin{pmatrix} \dot{\sigma} \\ -\dot{A} \end{pmatrix} = \begin{pmatrix} a^u & \bar{b} \\ \bar{b}^t & g \end{pmatrix} \begin{pmatrix} \dot{\varepsilon} \\ \dot{z} \end{pmatrix} \quad (10)$$

In a purely mechanical situation:

$$\dot{\sigma} = \sum_{j=1}^{N} \dot{\sigma}_j = \sum_{j=1}^{N} \left(p_0^j a^u \dot{\varepsilon} - \frac{\sigma^j - \sigma^{j,r}}{a(t)\tau_j^r} \right) \quad (11)$$

With

$$\dot{\sigma}^{j,r} = p_0^j a^u \dot{\varepsilon}\,,$$

$$\tau_j^r = \frac{h}{K_B T} \exp\left(\Delta F_j^{+,r}\right),$$

$$a(t) = \exp\left(\frac{K_\sigma \left| \sigma - \sigma^r \right|}{RT} \right).$$

where K_σ is homogeneous to an activation volume. The weight p_0^j of each mode is obtained by an extension of the fluctuation theory which leads to:

$$p_0^j = \frac{\sqrt{\tau^{j,r}}}{\sum_j \sqrt{\tau^{j,r}}} \quad (12)$$

where $\tau^{j,r}$ is the relaxation time of the j^{th} mode. Relaxation times $\tau^{j,r}$ distributed on 3 decades of the time scale according to $\tau^{j,r} = \tau^{max,r} 10^{-3(n-j)/(n-1)}$ where $\tau^{max,r}$ relates to the slowest process and n is the number of relaxation modes.

Among others authors, M.Loukil [14] and K. M'rabat [15] have worked on this model. Loukil described the state of the polymers in large deformations like a state governed by an elastic type law with the help of the Moony-Rivlin model, well enough adapted to the modelling of the elastomers. To characterize the constraint relaxed of the HDPE in large distortions experimentally, M'rabet did several sequences of relaxation from different load points situated in the traction domain. More lately, Arieby introduced the damaging effects in prevention of the behaviour of this material in large deformation.

III.2 Proposed Damage Model

Let's recall the meaningful progress of R. Arieby [16] concerning the characterization and the modelling of mechanical behaviour of the HDPE materials. In our case, we introduce the effective elastic modulus to describe damaging. In fact, contrarily to the R. Arieby model where the stress is measured using the real modulus E, we introduce a stress coupling to the damaging using the effective modulus E^{eff}:

$$\dot{\sigma}_1 = \sum_{j=1}^{N} \dot{\sigma}_1^j = E^{eff}\,\dot{\varepsilon}_1 - \sum_{j=1}^{N} \frac{\sigma_1^j - P_j^r \sigma_1^{j,r}}{\tau_j^r} \quad (13)$$

$$\dot{\sigma}_1^r = \sum_{j=1}^{N} \dot{\sigma}_1^{j,r} = E^{eff,r}\,\dot{\varepsilon}_1 - \sum_{j=1}^{N} \frac{\sigma_1^{j,r} - P_j^{eq} \sigma_1^{j,eq}}{\tau_j^{eq}} \quad (14)$$

To fully account for the dissipative nature of HDPE, the damage is integrated into both the instantaneous and relaxed states of the DNLR model. Eq. 15 defines the damaged relaxed modulus ($E^{eff,r}$), which governs the material's stiffness at equilibrium. In contrast, Eq. 16 describes the kinetic evolution of the effective instantaneous modulus (E^{eff}) as a function of strain, capturing the physical degradation caused by cavitation.

$$E^{r,eff} = E^r \left[1 - \left[\alpha_1 \left(1 - e^{-\beta_1 \varepsilon_1} \right) - \frac{1}{5} \chi L^{-1} \left(\frac{\lambda_C}{n^{0.5}} \right) \varepsilon_1 \right] \right] \quad (15)$$

$$E^{eff} = E \left[1 - \left[\alpha_1 \left(1 - e^{-\beta_1 \varepsilon_1} \right) - \frac{1}{5} \chi L^{-1} \left(\frac{\lambda_C}{n^{0.5}} \right) \varepsilon_1 \right] \right] \quad (16)$$

The equilibrium stress was approached by the 8 chains model of Arruda and Boyce [17], which is based on the statistical theory related to molecular chains.

In the case of uniaxial solicitation (tensile compression), this stress evolution obeys to the following expression:

$$\sigma_1^{eq} = \frac{N_{rl} K_B T}{3\lambda_C} n^{0.5} \left(\lambda_1^2 - \lambda_2^2 \right) L^{-1} \left(\frac{\lambda_C}{n^{0.5}} \right) \quad (17)$$

$$\lambda_1 = \exp(\varepsilon_1) \quad (18)$$

$$\lambda_2 = \frac{1}{\sqrt{\lambda_1}} \quad (19)$$

$$\lambda_C = \sqrt{\lambda_1^2 + \frac{2}{3}\lambda_2^2} \quad (20)$$

The model flexibility of Arruda and Boyce [17] lies in the possibility of reproducing the hardening led by stretching and reorientation of chains, in large deformations, by bringing in

only two parameters n and NKT. These last ones allow finding the global shape of the hyperelastic hardening.

The corresponding good values (listed below in the table) of these parameters were obtained after several simulations.

Table 1: Value of material parameters for HDPE

E (MPa)	E^r(MPa)	n	NKT (MPa)	α_1	β_1
1180	450	90	0.53	0.899	1 8

The equilibrium stress is supposed to interpret a reversible thermodynamic state; the figures 1, 2 and 3 illustrate the evolution of equilibrium stress to axial strain, the number n of segments per chain and the rubbery modulus parameter (NKT).

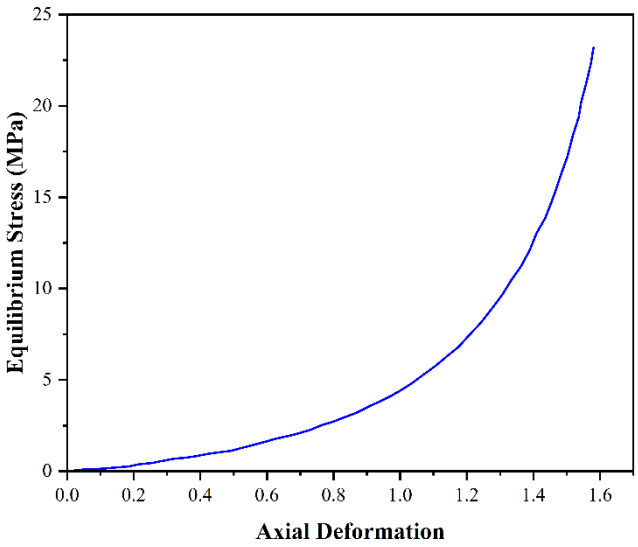

Figure 1: Evolution of equilibrium stress versus the axial strain

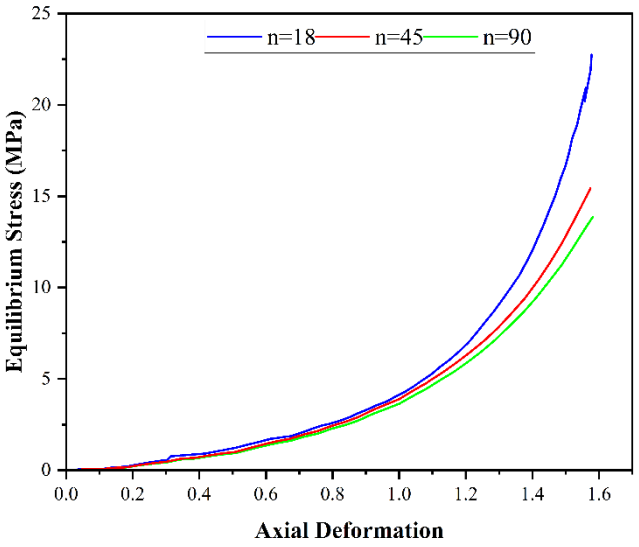

Figure 2: Influence of n on the equilibrium stress

Figure *2* illustrates the influence of the parameter (n) on the equilibrium stress response. According to the statistical theory of 8-chain networks, n dictates the limiting extensibility of the polymer chains. The results demonstrate that a lower value of (n) results in a higher stress response and a more rapid onset of hyperelastic hardening compared to higher values $(n = 90)$. This is physically consistent with the fact that shorter chains reach their maximum stretch more quickly, thereby increasing the material's resistance to further deformation.

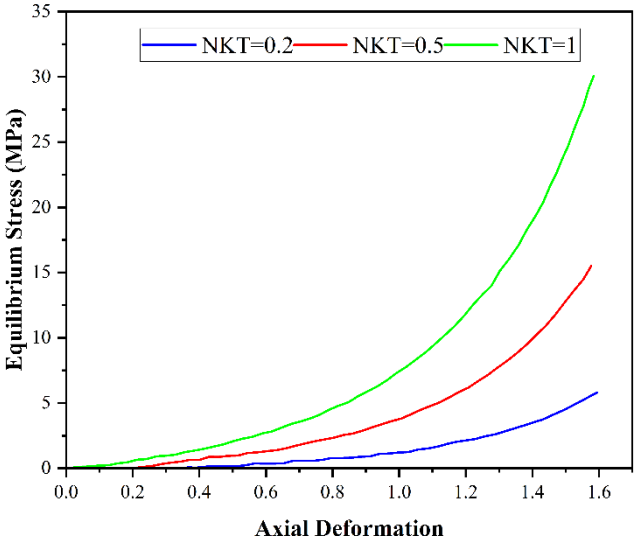

Figure 3: Influence of NKT on the equilibrium stress

The relaxation stress is defined by the equilibrium stress when $\tau^{eq} \ll \tau^{r}$. In figures 4, 5 and 6 demonstrate the influence of the relaxed Young's modulus (E_r), the chain segment parameter (n), and the damage magnitude coefficient (α_1) on the stress relaxation response, respectively.

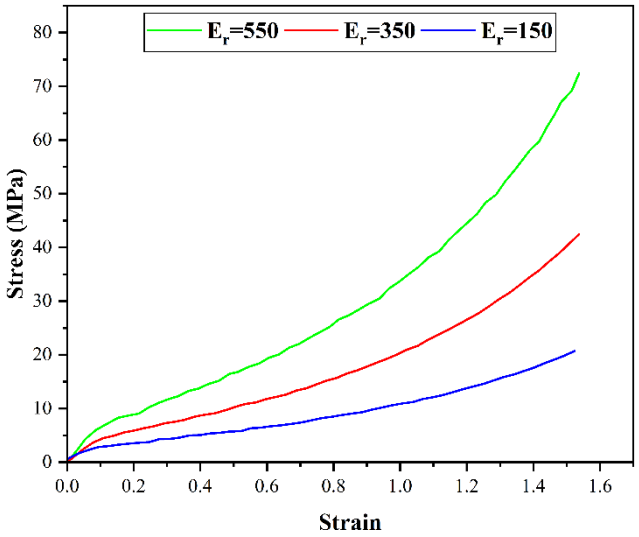

Figure 4: Influence of the relaxed modulus on the relaxed stress

Figure *4* depicts the sensitivity of the relaxation stress to variations in the initial relaxed Young's modulus (E_r). In the DNLR framework, E_r represents the stiffness of the material at the pseudo-equilibrium state once the viscous dissipative processes have subsided. The simulations show that a higher relaxed modulus ($E_r = 550\ MPa$) leads to a higher stress level across the strain range compared to a lower modulus ($E_r = 150\ MPa$). This alignment confirms that the stress response is directly proportional to the equilibrium stiffness of the macromolecular network, as required by thermodynamic consistency.

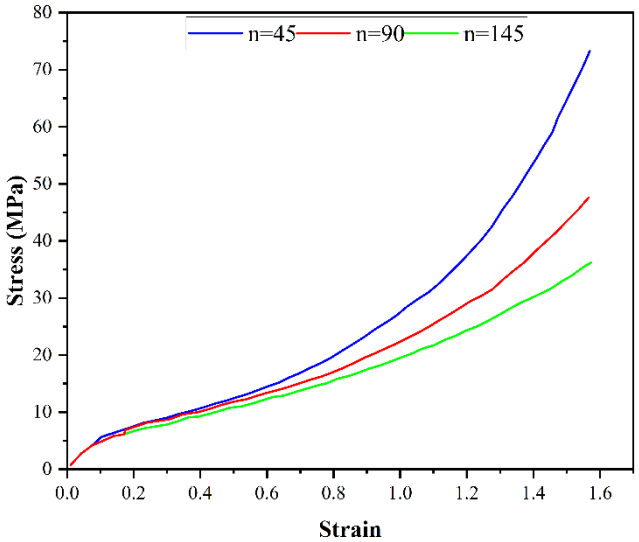

Figure 5: Effect of term n on the relaxed stress

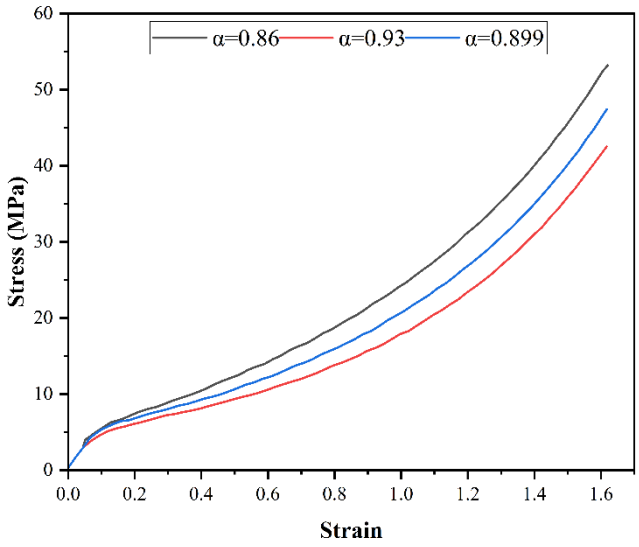

Figure 6: Effect of term α_1 on relaxed stress.

IV. Results and discussion

This study characterizes the evolution of damage in HDPE under uniaxial tension, with a specific focus on the variation of the Young's modulus as a function of strain [1], [8]. The results indicate that the apparent elastic modulus initially decreases sharply with axial deformation, reaching a limiting value of approximately 180 MPa due to the occurrence of cavitation damage [1]. Subsequently, the modulus enters a significant growth phase that progresses continuously until failure[6]. This recovery is attributed to the reorientation and stretching of macromolecular chains [2], [3], [6].

Despite the recovery of the Young's modulus at large strains, the value reached at failure does not return to its initial level. The numerical predictions of the proposed model demonstrate good agreement with the experimental results (see Fig. 7). A similar correlation is observed for the evolution of true stress as a function of strain (see Fig. 8).

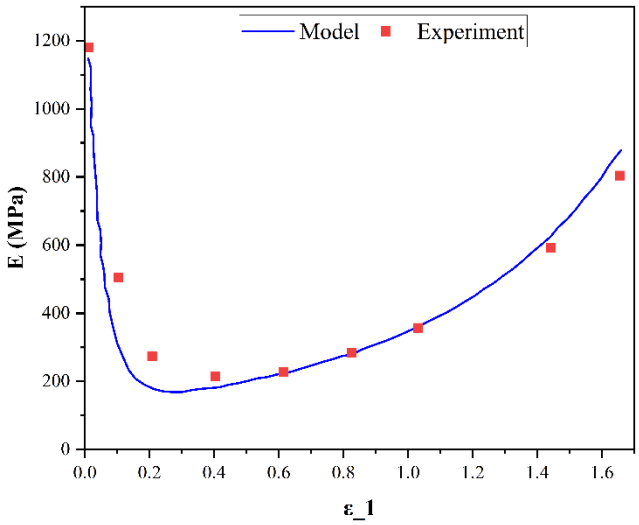

Figure 7: Evolution of the Young modulus, comparison of experimental and numerical results.

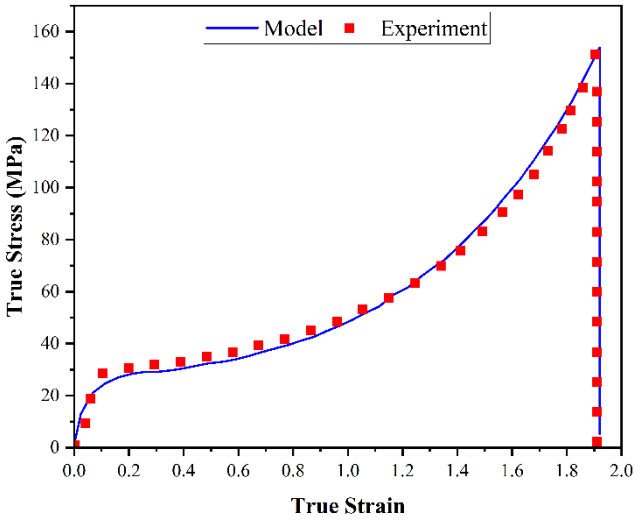

Figure 8: stress-strain curve, comparison of experimental and numerical results.

The quantitative assessment of the proposed DNLR formulation demonstrates a strong global reliability, as evidenced by a coefficient of determination (R^2) of 0.9486. This high value confirms that the model, when integrated with the Arruda and Boyce [17] eight-chain hyperelastic framework, successfully captures approximately 95% of the variance in the material's mechanical response during large plastic deformations [6]. The identification of precise material parameters was essential for this degree of correlation. The initial Young's modulus (E) of 1180 MPa represents the unrelaxed or instantaneous elastic response, while the relaxed Young's modulus (E^r) of 450 MPa reflects the pseudo-equilibrium stiffness of the material once viscous stresses have fully decayed [6].

Table 2: Statistical comparison numerical simulation vs experimental

$RMSE$	$RMSE(\%)$	MAE	MAE (%)	R^2
7.37	12.44%	3.108	5.24%	0.9486

The Mean Absolute Error (MAE) of 5.24% further validates the model's accuracy across the entire strain range, indicating that the numerical predictions closely follow the experimental stress-strain data [6], [8]. This average accuracy is largely supported by the model's ability to simulate hyperelastic hardening, which is governed by the number of rigid segments per chain ($n = 90$) and the rubbery modulus parameter ($NKT = 0.53MPa$) [6], [17]. The parameter is particularly critical as it dictates the limiting extensibility of the macromolecular network, marking the point where orientation-induced consolidation begins to significantly increase the material's resistance to further deformation [2], [3].

Localized deviations, reflected in the RMSE of 12.44%, likely occur during the complex transition between initial softening and final hardening, where localized phenomena like necking propagation are most intense [6], [16]. This phase is heavily influenced by the progression of internal damage, modeled here through the empirical parameters $\alpha_1 = 0.899$ and $\beta_1 = 18$. These coefficients effectively describe the total magnitude and the kinetics of cavitation and micro-void formation within the interlamellar amorphous domains [1], [6], [16]. Despite these minor fluctuations, the model accurately reproduces the characteristic "bathtub" evolution of the apparent elastic modulus, capturing the initial sharp stiffness loss down to a characteristic limiting value of approximately 180 MPa before the subsequent recovery induced by chain reorientation [1], [8].

V. Conclusions

In this work, we presented a constitutive framework based on the Distribution of Non-Linear Relaxation (DNLR) formalism, which establishes a rigorous link between the dissipative thermodynamics of relaxation in continuous media and the microscopic deformation physics of High-Density Polyethylene (HDPE). The primary contribution of this study is the development of a new model formulation that explicitly accounts for the evolution of internal damage and its coupling with the mechanical response.

The proposed model successfully reproduces the characteristic "bathtub" evolution of the apparent Young's modulus, capturing the sharp initial degradation down to a limiting value of approximately 180 MPa due to cavitation and micro-voiding, followed by a continuous recovery phase attributed to the reorientation and stretching of macromolecular chains. By integrating the statistical mechanics of the Arruda and Boyce (1993) eight-chain framework into the DNLR equilibrium state, the model provides a physically based description of hyperelastic hardening at large strains.

Numerical simulations demonstrated a high degree of quantitative accuracy, supported by a coefficient of determination (R^2) of 0.9486 and a Mean Absolute Error (MAE) of 5.24% when compared to experimental stress-strain data. The identified material parameters, including the initial modulus ($E = 1180MPa$), the number of segments per chain ($n = 90$), and the damage kinetics coefficients (α_1, β_1), are consistent with the known microstructural characteristics of semi-crystalline polymers. Ultimately, this unified thermodynamic approach proves to be a robust tool for predicting elastic-viscoplastic behavior and damage progression of thermoplastic polymers up to failure.

A. Acknowledgment:

This research received no specific grant from any funding agency in the public, commercial, or not-for-profit sectors.

***List of symbols**:*

$\boldsymbol{\sigma}$	*Observable mechanical stress.*
$\dot{\boldsymbol{\sigma}}$	*Stress rate.*
$\boldsymbol{\varepsilon}$	*True mechanical strain.*
$\dot{\boldsymbol{\varepsilon}}$	*strain rate.*
$\boldsymbol{A^j}$	*Thermodynamic affinity associated with the j^{th} relaxation mode.*
$\boldsymbol{z^j}$	*Internal variable representing the degree of advancement of the j^{th} dissipative process.*
$\boldsymbol{\psi_k}$	*Generalized thermodynamic potential (free energy).*
$\boldsymbol{T}$	*Absolute Temperature (°K).*
$\boldsymbol{s}$	*Specific entropy.*
$\boldsymbol{a^u}$	*Instantaneous stability tensor / the Tisza matrix.*
$\overline{\boldsymbol{b}}$	*Rectangular coupling tensor between reversible and irreversible state variables.*
$\boldsymbol{g}$	*Internal stability tensor / dissipation matrix.*
$\boldsymbol{\tau_j^r}$	*Reference relaxation time of mode in the relaxed state.*
$\boldsymbol{a(t)}$	*Time-dependent non-linearity factor / sliding factor.*
$\boldsymbol{P_0^j}$	*Statistical weight of the j^{th} relaxation mode.*
$\boldsymbol{E}$	*Initial Young's modulus.*
$\boldsymbol{E^r}$	*Initial Young's modulus at the relaxed state.*
$\boldsymbol{E^{eff}}$	*Effective (damaged) Young's modulus.*
$\boldsymbol{E^{eff,r}}$	*Effective Young's modulus at the relaxed state.*
$\boldsymbol{D}$	*Scalar damage variable.*
$\boldsymbol{\alpha_1}$	*Parameter characterizing the maximum damage level by cavitation.*
$\boldsymbol{\beta_1}$	*Parameter characterizing the damage saturation rate.*
$\boldsymbol{\chi}$	*Parameter related to macromolecular chain reorientation.*
$\boldsymbol{n}$	*Number of rigid segments per macromolecular chain.*
$\boldsymbol{NKT}$	*Rubbery modulus parameter related to chain density.*
$\boldsymbol{\lambda_c}$	*Internal stretch of a localized network chain.*
$\boldsymbol{\lambda_1, \lambda_2}$	*Principal stretch ratios.*
$\boldsymbol{L^{-1}}$	*Inverse Langevin function.*
$\boldsymbol{k_B}$	*Boltzmann constant.*

***References**:*

1. R. Arieby, Caractérisation mécanique et modélisation thermodynamique du comportement anisotrope du polyéthylène à haute densité. Intégration des effets d'endommagement, Doctorat ès Mécanique et énergétique, PhD, Vandoeuvre-les-Nancy, INPL, 2007. https://doi: 10.70675/e9cba821zc722z40e7z906ez7b40c7b255

2. R. Rahouadj, K. M'Rabet, R. Arieby, et C. Cunat, Sur le couplage des mécanismes de déformation intervenant dans le comportement élasto-visco-plastique du PEHD, présenté à CFM 2007 - 18ème Congrès Français de Mécanique, AFM, Maison de la Mécanique, 39/41 rue Louis Blanc - 92400 Courbevoie, août 2007. Consulté le: 6 juin 2026. [En ligne]. Disponible sur: https://hal.science/hal-03365572

3. A. Peterlin, Molecular model of drawing polyethylene and polypropylene, Journal of Materials Science, vol. 6, n° 6, p. 490‑508, juin 1971, https://doi.org/10.1007/BF00550305

4. A. Keller, Polymer crystals. Reports on Progress in Physics. Vol 3; n° 2, 623-704, 1968, https://doi: 10.1088/0034-4885/31/2/304.

5. K. Saalwächter, T. Thurn-Albrecht, et W. Paul, Recent Progress in Understanding Polymer Crystallization, Macromolecular Chemistry and Physics. vol. 224, n° 7, p. 2200424, 2023, https://doi:10.1002/macp.202200424

6. R. Ferhoum, M. Aberkane, et M. Ould Ouali, Distribution of nonliner relaxation (DNLR) approach of the annealing effects in semicristalline polymers: structure–property relation for high-density polyethylene (HDPE), Continuum Mechanics and Thermodynamics. vol. 26, n° 3, p. 373-385, 2014. https://doi:10.1007/s00161-013-0306-9

7. I. M. Ward, Review: The yield behaviour of polymers, Journal of Materials Science. Vol 6, 1397-1417,1971. https://doi.org/10.1007/BF00549685

8. K. Hachour, R. Ferhoum, M. Aberkane, F. Zairi, et M. N. Abdelaziz, Experimental Characterization and Effect of the Triaxiality on the Behavior of the HDPE, in *Damage* and Fracture Mechanics: Failure Analysis of Engineering Materials and Structures, T. Boukharouba, M. Elboujdaini, et G. Pluvinage, Éd., Dordrecht: Springer Netherlands, 2009, p. 43-48. https://doi: 10.1007/978-90-481-2669-9_5.

9. Z. Bartczak, Deformation of semicrystalline polymers - the contribution of crystalline and amorphous phases, Polimery, vol. 62, n° 11-12, p. 787-799, 2017, https://doi: 10.14314/polimery.2017.787.

10. C. Cunat, Thermodynamic Treatment of Relaxation in Frozen-In Systems. Universality of the Distribution Law for Relaxation Times, Zeitschrift für Physikalische Chemie, vol. 157, n° 1, p. 419-423, janv. 1988, https://doi: 10.1524/zpch.1988.157.Part_1.419.

11. C. Cunat, The DNLR Approach and Relaxation Phenomena. Part I – Historical Account and DNLR Formalism, Mechanics of Time-Dependent Materials, Vol 5, 39-65, 2001, https://doi: 10.1023/a:1009899519935.

12. M. Loukil, Modélisation des surfaces de plasticité à partir d'une approche de la thermodynamique de la relaxation des milieux continus, phdthesis, Institut National Polytechnique de Lorraine, 1996. Consulté le: 6 juin 2026. [En ligne]. Disponible sur: https://hal.univ-lorraine.fr/tel-01751159

13. S. André, N. Renault, Y. Meshaka, et C. Cunat, From the thermodynamics of constitutive laws to the thermomechanical experimental characterization of a semicrystalline polymer from IR imaging, Continuum Mechanics and Thermodynamics, Vol 24, 1-20, 2012. https://doi.org/10.1007/s00161-011-0205-x

14. L. Rabemananjara, Etude de l'influence de la vitesse de déformation sur la réponse à l'indentation des matériaux polymères, Theses, Université de Rennes, 2015. Consulté le: 6 juin 2026. [En ligne]. Disponible sur: https://theses.hal.science/tel-01285396

15. A. Blaise, S. André, P. Delobelle, Y. Meshaka, et C. Cunat, Advantages of a 3-parameter reduced constitutive model for the measurement of polymers elastic modulus using tensile tests, Mechanics of Time-Dependent Materials. vol. 20, n° 4, p. 553-577, nov. 2016, https://doi: 10.1007/s11043-016-9312-1.

16. R. Ferhoum, M. Aberkane, et K. Hachour, Analysis of thermal ageing effect (hold time-crystallinity rate-mechanical property) on high density polyethylene (HDPE), International Journal of Materials Science, vol. 2, n° 3, Art. n° 3, 2014. https://doi:10.11648/j.ijmsa.20130203.17

17. E. M. Arruda et M. C. Boyce, A three-dimensional constitutive model for the large stretch behavior of rubber elastic materials, Journal of the Mechanics and Physics of Solids, vol. 41, n° 2, Art. n° 2, 1993. https://doi:10.1016/0022-5096(93)90013-6

Biopolymer Applications Journal ***Rebiha Bellache et al. Vol 5 N°2, 2026, pp. 16-20***
e-ISSN: 2800-1729

Formulation and characterization of oil/water emulsions stabilized by biopolymer complexes

Rebiha Bellache[1,2*] ; Dalila Hammiche[2]
[1]*Université M'Hamed Bougara de Boumerdès, Faculté de Technologie, Département de Génie des Procédés, Boumerdès 35000, Algérie*
[2]*Université de Bejaia, Faculté de Technologie, Laboratoire des Matériaux Polymères Avancés Route De Targa- Ouzemmour, Bejaia 06000, Algérie*
**Corresponding author email: r.bellache@univ-boumerdes.dz*
Received: 13 June 2026; Accepted: 1 July 2026; Published: 13 July 2026

Abstract

Emulsions are thermodynamically unstable colloidal systems consisting of two immiscible liquids. To overcome the use of potentially irritating synthetic surfactants, this study evaluates the stabilization of simple oil/water emulsions using natural biopolymers, specifically proteins and polysaccharides. Emulsions were formulated using olive oil and mixtures of chitosan, starch, and mycological peptone. The influence of pH (2, 3, and 4) on the formation of biopolymer complexes was investigated. Macroscopic and microscopic characterizations revealed that the emulsion stabilized by the chitosan/protein complex at pH 4 exhibited the best physical stability. This stability was manifested by the absence of phase separation, sedimentation, and coalescence. UV-Visible spectrophotometry analyses showed a maximum absorbance at this pH, indicating maximal interaction between the macromolecules. Finally, infrared spectroscopy confirmed the formation of physical interactions between the protein and the polysaccharide, leading to a perfectly homogeneous phase. The chitosan/protein emulsion at pH 4 demonstrated superior stability, maintaining a homogeneous structure without phase separation, unlike the unstable chitosan/starch emulsions. FTIR analysis revealed strong interactions between chitosan and protein, evidenced by changes in the O–H, C–H, and C=O bands, whereas the unstable emulsions showed no significant spectral changes, indicating a lack of intermolecular interactions.
Keywords: *Biopolymers, Chitosan, Emulsion, Protein, Stability*

I. Introduction

Emulsions are constantly present in our daily life and are encountered in numerous fields, including the pharmaceutical, cosmetic, food, paint, agrochemical, and petroleum industries [1]. In the pharmaceutical industry, applications are numerous, such as parenteral emulsions, topical emulsions, and oral or ophthalmic emulsions [2]. The term emulsion refers to a colloidal system comprising at least two immiscible liquids (usually water and oil), where one liquid is dispersed as small droplets in a continuous phase constituted by the other liquid, in a more or less stable form. Droplet size varies depending on conditions, from 0.1 to a few tens of micrometers [1].

Emulsions are thermodynamically unstable systems, and their stability is ensured by the presence of emulsifiers or stabilizers. To overcome the use of potentially irritating synthetic surfactants, natural biopolymers such as proteins and polysaccharides have gained interest as effective emulsifiers and stabilizers due to their surface activity and gelling properties [3]. Many proteins can act as emulsifiers because of their ability to adsorb at the oil-water interface. Some polysaccharides also possess surface activity and are capable of stabilizing emulsions by adsorbing at the interface between the two liquids [4].

Furthermore, the complexation between polysaccharides and proteins, often driven by electrostatic interactions between oppositely charged macromolecules, can lead to improved emulsion stability. The formation of soluble or insoluble complexes depends on pH and ionic strength [5]. These biopolymer complexes not only enhance physical stability against coalescence and flocculation but also offer controlled release and encapsulation benefits for bioactive compounds [6]. Recent advances have demonstrated their potential in designing clean-label food products and biocompatible pharmaceutical formulations [7]. According to et al [8] Biopolymer-based nanocarriers, such as nanoparticles, nanoemulsions, nanoliposomes, micelles, and nanofibers, effectively encapsulate phenolic compounds like quercetin, curcumin, catechin, and resveratrol, enhancing their solubility, stability, and biological effectiveness for targeted therapeutic and nutraceutical applications.
This study focuses on the stabilization of simple oil-in-water emulsions using biopolymer complexes. The specific objectives are to formulate emulsions with olive oil as the active lipophilic phase and mixtures of chitosan (cationic polysaccharide), starch (neutral polysaccharide), and mycological peptone (protein), and to investigate the influence of pH (2, 3, and 4) on the formation and stability of

these biopolymer complexes. The novelty of this study lies in the first-time association of mycological peptone with chitosan to develop a stable emulsion through enhanced intermolecular interactions. Physicochemical characterizations, including macroscopic and microscopic observations, UV-Visible spectrophotometry to predict zones of maximal interaction, and infrared spectroscopy to identify molecular interactions, are performed to evaluate emulsion stability.

II. Material and methods

II.1 Materials

Olive oil was selected as the dispersed (lipophilic) phase. Its main physicochemical properties include a dynamic viscosity of 0.1 Pa·s at 20°C and insolubility in water. The stabilizing agents tested included polysaccharides such as chitosan (cationic, molecular weight 100,000-300,000, soluble in acidic media), commercial starch and synthesized starch, as well as a protein (mycological peptone, a yellowish powder soluble in water, pH 5-7 at 2% w/v). The surfactants PEG 600 (hydrophilic) and Span 80 (lipophilic) were used during emulsification. Hydrochloric acid (1N HCl) was used for pH adjustment, and distilled water served as the aqueous phase.

II.2 Preparation of polymeric solutions

Biopolymer mixtures were prepared by combining 50 mL of a 0.2% chitosan solution with 40 mL of 0.2% starch or protein, supplemented with the active ingredient (olive oil) and the homogenization speed was 10,000 rpm. The temperature of the mixture was maintained at 50 °C for 30 minutes. The pH of these solutions was then adjusted to target values of 2, 3, or 4 by adding hydrochloric acid (1N HCl). Three mixtures were prepared: Mixture 1 (chitosan + commercial starch), Mixture 2 (chitosan + mycological peptone), and Mixture 3 (chitosan + synthesized starch).

II.3 Emulsification

The aqueous phase (containing the hydrophilic surfactant PEG) was mixed with the oily phase (containing Span 80 and olive oil). Final homogenization was carried out using a mixer under strong agitation for 5 minutes to reduce droplet size.

II.4 Physico-chemical characterizations

- Macroscopic and microscopic appearance: Visual evaluation of homogeneity (phase separation, sedimentation) and observations under a light microscope (x40 magnification; scale bar = 100 µm) to identify instabilities such as coalescence or flocculation.
- UV-Visible spectrophotometry: Absorbance measurement between 200 and 500 nm to evaluate turbidity and predict zones of maximal interaction between macromolecules. Measurements were performed using a PerkinElmer Lambda 25 spectrophotometer.
- Infrared (IR) spectroscopy: Determination of the effect of pH on chemical bonds and interactions between macromolecules, using a PerkinElmer FT-IR spectrometer.

Table 1: Macroscopic and microscopic appearance of 9 emulsions of different pH

Biopolymer blends (9 tests)	9 emulsions PH=2 ; 3 ; 4	Macroscopic aspect	Observation	Microscopic aspect	Observation
Blend (chitosan and commercial starch)	Emulsion 1 pH=2		A phase separation	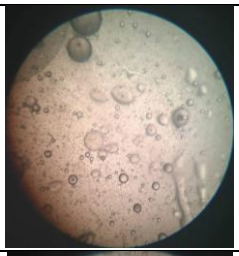	Presence of small globules
	Emulsion 1 pH=3	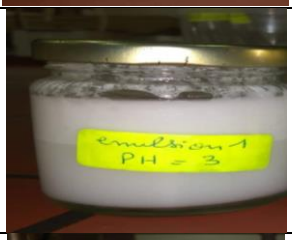	A phase separation	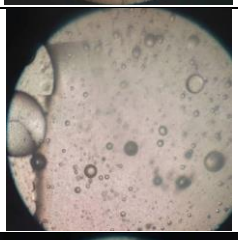	Presence of globules of different sizes: small, medium, and large; therefore, no homogeneity of the globules.
	Emulsion 1 pH=4		A phase separation	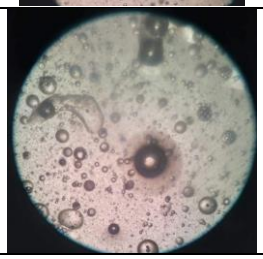	Presence of globules of different sizes: small, medium, and large; therefore, no homogeneity of the globules.

Blend (chitosan and mycological peptone)	Emulsion 2 pH=2		Homogeneous blend	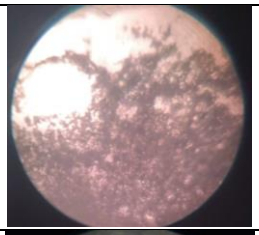	The size of the globules is homogeneous.
	Emulsion 2 pH=3	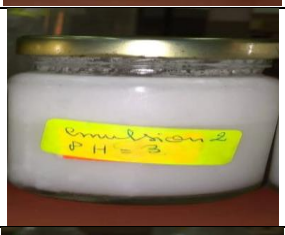	Homogeneous blend	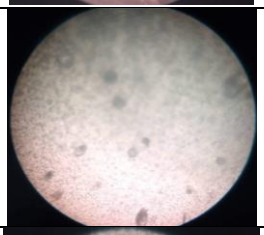	The size of the globules is homogeneous.
	Emulsion 2 pH=4		Homogeneous blend	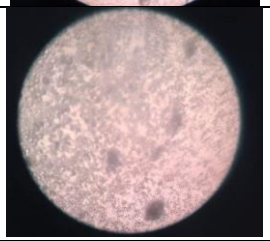	The size of the globules is homogeneous.
Blend (chitosan and synthesized starch)	Emulsion 3 pH=2		A phase separation	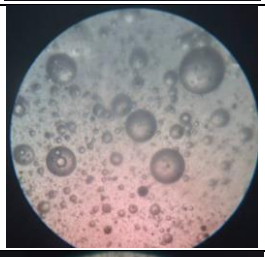	Presence of globules of different sizes: small, medium, and large; therefore, no homogeneity of the globules.
	Emulsion 3 pH=3		A phase separation	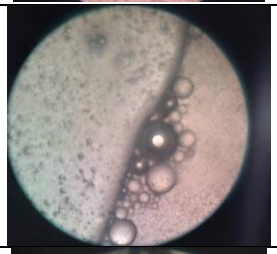	Presence of globules of different sizes: small, medium, and large; therefore, no homogeneity of the globules.
	Emulsion 3 pH=4		A phase separation	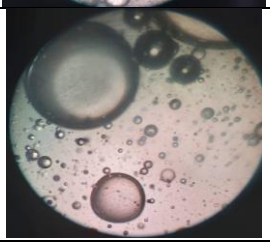	Presence of globules of different sizes: small, medium, and large; therefore, no homogeneity of the globules.

III. Results and discussion

III.1 Macroscopic and microscopic characterization

The visual examination in table 1 revealed that emulsions 1 (chitosan/commercial starch) and 3 (chitosan/synthesized starch) exhibited phase separation (sedimentation) for all studied pH values (2, 3, and 4). This opaque appearance indicates low solubility and instability of the polysaccharide complex, likely due to weak electrostatic interactions leading to liquid-liquid or liquid-solid phase separation [9]. Conversely, emulsion 2 (chitosan/protein) showed a perfectly homogeneous mixture at pH 2, 3, and 4.

Microscopic analysis confirmed that emulsion 2 formulated at pH 4 provided the best long-term physical stability. The globules had a homogeneous size, with no signs of flocculation or coalescence, unlike the other samples which destabilized quickly. Emulsion 2 at pH 4 remained stable for four weeks, whereas emulsions 1 and 3 destabilized within one day. This stability is attributed to optimal electrostatic interactions between positively charged chitosan and negatively charged protein at pH 4 (below the isoelectric point of the protein) [10].

Our results agree with previous reports on chitosan–protein complexes, where enhanced emulsifying properties under

acidic conditions were attributed to strong intermolecular interactions and smaller particle sizes. Likewise, the chitosan–mycological peptone emulsion exhibited excellent stability at pH 4, supporting the hypothesis that complex formation promotes homogeneous dispersion and prevents phase separation, while introducing mycological peptone as a novel protein component for stabilizing chitosan-based emulsions [11].

III.2 UV-Visible spectrophotometry

The UV-Visible graph in figure 1 of the sediments highlighted an absorbance peak at pH 4 for biopolymer mixture 2 (protein/chitosan). This maximal value reflects increased turbidity, demonstrating that electrostatic interactions between the two macromolecules are at their maximum under these pH conditions [12]. The absorbance values for the individual biopolymers in Table 2 confirmed their intrinsic optical properties.

Table 2: The absorbances of the different biopolymers

biopolymers	Absorbance	Wavelength (cm^{-1})
Commercial starch	2.505	283
Synthesized starch	2.505	280
Protein	2.505	282
Chitosan	2.505	270.5

III.3 Infrared (IR) spectroscopy

The IR spectra of the stable emulsion (chitosan/protein) showed (figure 2) a decrease in the O-H absorption band and an increase in the intensity of the C-H and C=O bands. The glycosidic C–O–C stretching vibration of starch (1020-1080 cm^{-1}) showed slight changes in intensity after complex formation, suggesting interactions between polysaccharide hydroxyl groups and chitosan [13]. These variations prove the presence of branching and strong physical interactions between the protein and chitosan chains, which explains the homogeneity of the obtained phase. For unstable emulsions, the intensity of the bands remained unchanged due to the absence of attractive interactions between the polysaccharides [14].

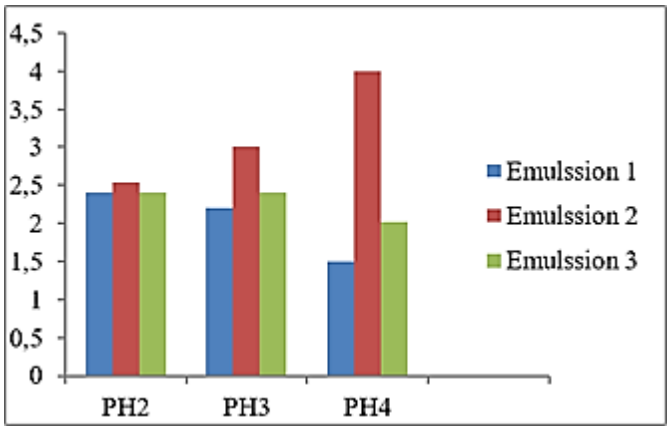

Figure 1: UV-visible graph of all the emulsions

IV. Conclusions

This study highlighted the crucial role of biopolymer complexes as stabilizers for simple oil/water emulsions. The combination of chitosan and mycological peptone at a pH of 4 resulted in the most physically stable emulsion. Microscopic characterizations, coupled with spectroscopic analyses (UV-Visible and IR), confirmed the absence of coalescence and the presence of strong structural interactions between the macromolecules. The choice of a common vegetable oil (olive oil) did not alter the stability, thus offering very promising perspectives for applications in the field of galenic pharmacy.

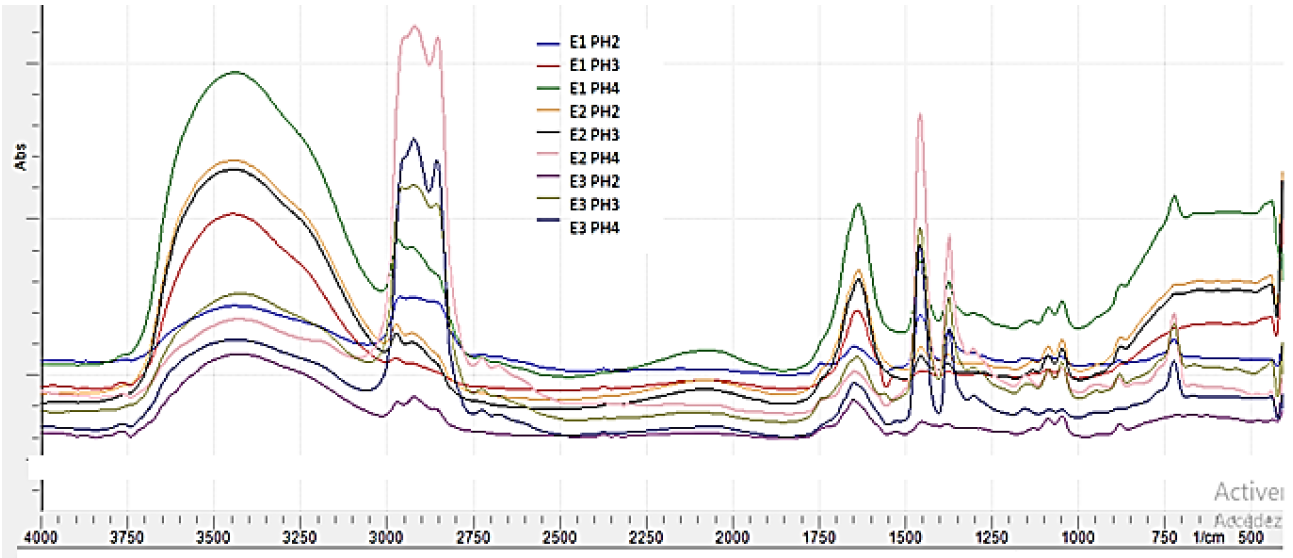

Figure 2: Infrared spectrum of all the emulsions

Acknowledgment*:*
The authors would like to thank the students HASSANI Yasmine et AMRIOUI Chanese For the realization of this work.

References:

1. J. McClements. Emulsion design to improve the delivery of functional lipophilic components. Annual Review of Food Science and Technology 1, 241-269, 2010. https://doi.org/10.1146/annurev.food.080708.100722
2. C. Chung, D. J. McClements. Structure-function relationships in food emulsions: improving food quality and sensory perception. Food Structure 1(2), 106-126, 2014. https://doi.org/10.1016/j.foostr.2013.11.002
3. S. L. Turgeon, M. Beaulieu, C. Schmitt, C. Sanchez. Protein–polysaccharide complexes: from fundamentals to food applications. Current Opinion in Colloid & Interface Science 8(4), 401-414, 2003. https://doi.org/10.1016/S1359-0294(03)00093-X
4. C. Schmitt, S. L. Turgeon. Protein/polysaccharide complexes and coacervates in food systems. Advances in Colloid and Interface Science 167(1-2), 63-70, 2011. https://doi.org/10.1016/j.cis.2010.10.001
5. T. F. Tadros. Emulsion formation, stability, and rheology. In T. F. Tadros (Ed.), Emulsion formation and stability. Wiley-VCH, Weinheim, pp 1-75, 2013.
6. C. Qiao, L. Gu, D. Xu, X. Yang, Y. Wang. Protein-polysaccharide complexes: From fundamentals to food applications. Food Hydrocolloids 117, 106728, 2021. https://doi.org/10.1080/87559129.2025.2609585
7. M. Esfanjani, S. M. Jafari. Biopolymer nano-particles and natural nano-carriers for nano-encapsulation of phenolic compounds. Food Hydrocolloids 146, 532-543, 2016. https://doi.org/10.1016/j.colsurfb.2016.06.053
8. C. Yan, D. J. McClements, Y. Zhu, L. Zou, W. Zhou, W. Liu. Fabrication of OSA Starch/Chitosan Polysaccharide-Based High Internal Phase Emulsion via Altering Interfacial Behaviors. Journal of Agricultural and Food Chemistry 67(39), 10937-10946, 2019. https://doi.org/10.1021/acs.jafc.9b04009
9. A. Tiwari, V. Tiwari, Nanotechnology for Polyphenol Delivery and Applications, in: Exploring the Synthesis, Ethnopharmacology, and Therapeutic Applications of Bioactive Polyphenols, 1st ed., CRC Press, Boca Raton, 2026: pp. 184–194. https://doi.org/10.1201/9781003564300-15.
10. Ye. Complexation between milk proteins and polysaccharides via electrostatic interaction: principles and applications – a review. International Journal of Food Science & Technology 43(3), 406-415, 2008. https://doi.org/10.1111/j.1365-2621.2006.01454.x
11. Y. Lang, M. Wang, S. Zhou, D. Han, P. Xie, C. Li, X. Yang. Fabrication, characterization and emulsifying properties of myofibrillar protein-chitosan complexes in acidic conditions. International Journal of Biological Macromolecules, 262(2), 2024. https://doi.org/10.1016/j.ijbiomac.2024.130000
12. K. W. Mattison, I. J. Brittain, P. L. Dubin. Protein-Polyelectrolyte Phase Boundaries. Biotechnology Progress 11(6), 632-637, 1995. https://doi.org/10.1021/bp00036a005
13. R. Milusheva, O. Avazova, S. Rashidova. Polymolecular Complexes of Chitosan with the Bombyx Mori Protein. Chemistry of Natural Compounds 58, 364-367, 2022. https://doi.org/10.31489/2022Ch3/3-22-22
14. Y. Lang, et al. Fabrication, characterization and emulsifying properties of myofibrillar protein-chitosan complexes in acidic conditions. International Journal of Biological Macromolecules 262(Pt2), 130000, 2024. https://doi.org/10.1016/j.ijbiomac.2024.130000

iopolymer Applications Journal
e-ISSN: 2800-1729

Hayet Ahlem Lezrag et al. Vol 5 N° 2, 2026, pp. 21-29

Niosomal Encapsulation of *Artemisia herba-alba* Essential Oil: Optimization and Characterization Using Box-Behnken Design

Hayet Ahlem Lezrag[1. 2. 3*] ; Sofiane Fatmi[1. 2. 4*] ; Zahra Toutou[1. 2] ; Katarzyna Pokajewicz[3] ; Mohamed Skiba[4] ; Piotr P. Wieczorek[3] and Mokrane Iguerouada[1]

1: Université de Bejaia. Faculty of Nature and Life Sciences. Associated Laboratory in Marine Ecosystems and Aquaculture. 06000 Bejaia. Algeria
2: Université de Bejaia. Faculty of Technology. Technology Pharmaceutical Laboratory. 06000 Bejaia. Algeria.
3: University of Opole. Institute of Chemistry. 45-052 Opole. Poland.
4: Technology Pharmaceutical and Bio Pharmaceutics Laboratory. UFR Medicine and Pharmacy. Rouen University. 22 Blvd. Gambetta. 76183. Rouen. France.
**Corresponding author email: sofiane.fatmi@univ-bejaia.dz, hayetahlem.lezrag@univ-bejaia.dz*

Received: 9 June 2026; Accepted: 1 July 2026.; Published: 13 July 2026

Abstract

This study focuses on the development and optimization of niosomal vesicles for the encapsulation of Artemisia herba-alba (white wormwood) essential oil, a plant native to arid and semi-arid regions of Algeria. A Box-Behnken experimental design was employed to investigate the effects of cholesterol concentration, Span 60 concentration, and sonication time on niosome size and encapsulation efficiency. The optimal formulation was achieved using 0.25 µL/mL of essential oil, 2.5 mg/mL of cholesterol, 5.8 mg/mL of Span 60, and a sonication time of 7 min, resulting in an experimental encapsulation efficiency of 90.67% with an average particle size of 880 nm. Fourier-transform infrared spectroscopy (FTIR) confirmed the physical nature of encapsulation through hydrogen bonding interactions without chemical modification of components. X-ray diffraction (XRD) analysis revealed a decrease in crystallinity of excipients, indicating successful integration of the essential oil into the niosomal bilayer. Stability studies demonstrated progressive physical instability with particle growth from 880 nm to 2780 nm over 90 days, while encapsulation efficiency remained above 83%. These findings establish niosomes as an effective vectorization system for A. herba-alba essential oil, enhancing its stability and offering promising applications in pharmaceutical and nutraceutical fields.

Keywords: *Artemisia herba-alba, essential oil, niosomes, Box-Behnken design, FTIR, XRD.*

I. Introduction

Essential oils represent a valuable source of bioactive compounds with demonstrated antimicrobial, antioxidant, anti-inflammatory, and therapeutic properties [1]. Among aromatic and medicinal plants. Artemisia herba-alba Asso (white wormwood, Asteraceae) occupies a prominent position in traditional medicine across North Africa and the Mediterranean basin. This perennial shrub, characteristic of arid and semi-arid steppic ecosystems. produces an essential oil rich in oxygenated monoterpenes, particularly camphor (39.5%), chrysanthenone (10.4%), and 1.8-cineole (8.6%) alongside α-thujone (7.0%) and borneol (3.4%) [2]. These terpenic compounds confer potent antioxidant. antibacterial. antifungal, and anti-inflammatory activities [3].

Despite their therapeutic potential, essential oils present significant limitations that restrict their pharmaceutical applications high volatility, poor water solubility, chemical instability under environmental stressors (light, oxygen, temperature), and potential toxicity at elevated concentrations [4]. These constraints necessitate the development of advanced drug delivery systems capable of protecting. stabilizing, and controlling the release of these bioactive molecules.

Niosomes (non-ionic surfactant vesicles) have emerged as promising nanocarriers for the encapsulation of both hydrophilic and lipophilic compounds [5]. Composed of non-ionic surfactants (typically Span series) and cholesterol, niosomes offer several advantages over conventional liposomes enhanced chemical stability, lower production costs, absence of special storage requirements, and reduced toxicity [6]. Their bilayer structure enables the encapsulation of lipophilic compounds such as essential oils within the hydrophobic membrane domain, thereby improving solubility. bioavailability and controlled release [7].

The optimization of niosomal formulations requires systematic evaluation of multiple formulation variables. Response surface methodology (RSM), particularly the Box-Behnken design (BBD). Provides an efficient statistical approach for studying the effects of independent variables and their interactions on multiple responses with a reduced number of experimental runs [8]. This design has been successfully applied to optimize niosomal formulations for various drugs and natural compounds [9.10].

The present study aims to develop and optimize niosomal formulations for A. herba-alba essential oil using BBD,characterize the optimized formulation through FTIR spectroscopy and XRD analysis and evaluate the stability of niosomal vesicles during storage.

This work represents, to our knowledge, the first systematic optimization of niosomal encapsulation for Algerian A. herba-alba essential oil using a quality-by-design approach.

II. Material and methods

II.1. Materials

Artemisia herba-alba essential oil was obtained by hydrodistillation of aerial parts collected in the region of Bordj Bou Arreridj, Northeastern Algeria. during the flowering stage, Span 60 (sorbitan monostearate) and cholesterol were purchased from Sigma-Aldrich (St. Louis. MO. USA). Absolute ethanol. were obtained from Biochem Chemopharma (Canada). All reagents were of analytical grade.

II2. Isolation of essential oil from Artemisia herba-alba

Artemisia herba-alba. commonly known as white wormwood. is a plant species native to arid and semi-arid regions. The fresh aerial parts of A. herba-alba were collected in Northeastern Algeria. specifically in the region of Bordj Bou Arreridj. during the flowering stage. After harvesting. The plant material was roughly chopped, air-dried, and then subjected to hydrodistillation for 4 hours using a Clevenger-type apparatus. The resulting essential oil was collected and stored at 4 °C in the dark until further analysis and experimental use [11].

II.3. Preparation of niosomal formulations

Niosomes were prepared using the ethanol injection method [12]. Briefly, Span 60, cholesterol. and A. herba-alba essential oil were dissolved in absolute ethanol to form the organic phase. This solution was maintained under magnetic stirring at 60 °C for 20 min to ensure complete dissolution. The organic phase was then injected into the aqueous phase (preheated to 60 °C) using a syringe. with continuous stirring. Residual ethanol was removed by rotary evaporation under reduced pressure. The resulting suspension was sonicated using a bath sonicator (Sonitech. ST-80 PRO) for the designated time period to obtain homogeneous niosomes.

II.4. Box-Behnken experimental design

Optimization of the niosomal formulation was carried out using a three-factor, three-level Box–Behnken design (BBD) implemented in MODDE 6.0 software (Umetrics AB, Sweden) [13]. Cholesterol concentration (X_1, 1–5 mg/mL), Span 60 concentration (X_2, 5–15 mg/mL), and sonication time (X_3, 2–7 min) were selected as independent variables based on their expected influence on vesicle formation and stability. Encapsulation efficiency (Y_1, %) and particle size (Y_2, nm) were chosen as response variables to evaluate formulation performance. The design generated a total of 15 experimental combinations, including three center-point replicates, allowing estimation of pure error, evaluation of model adequacy, and assessment of experimental reproducibility. The actual and coded values of the investigated factors are presented in Table 1.

Table 1. Variables and levels in Box-Behnken design

Factor	Symbol	Units	Low (-1)	Center (0)	High (+1)
Cholestérol	Cho (X_1)	mg/mL	1	3	5
Span 60	Spa (X_2)	mg/mL	5	10	15
Sonication time	Son (X_2)	min	2	4.5	7

II.5. Niosome size determination

The particle size of the niosomal suspensions was determined by optical microscopy using an ocular micrometer calibrated with an objective micrometer. Briefly, a drop of the niosomal suspension was placed on a clean microscope slide and covered with a coverslip. The calibrated ocular micrometer enabled direct measurement of vesicle diameters, with the micrometric divisions converted into length units using the established calibration factor. For each formulation, the diameters of at least 100 individual vesicles were measured to ensure statistical reliability, and the mean particle size was subsequently calculated [13].

II.6. Characterization of optimized formulation

II.6.1 Determination of encapsulation efficiency

Encapsulation efficiency (EE) was determined using a centrifugation-based separation method. The niosomal suspensions were centrifuged at 15,000 rpm for 90 min at 4 °C to ensure efficient separation of vesicles from the non-encapsulated essential oil. The low temperature was maintained to minimize the volatilization and potential degradation of the essential oil components during centrifugation. Following centrifugation, the supernatant

containing the free (non-encapsulated) essential oil was carefully collected and removed The resulting pellet [13]. Corresponding to the niosomal fraction, was dissolved in ethanol to disrupt the vesicular structure and release the encapsulated essential oil. The amount of encapsulated oil was then quantified by UV-visible spectrophotometry at 287 nm using a previously established calibration curve. Encapsulation efficiency was calculated according to the following equation:

$$EE\ (\%) = \frac{\text{Amount of encapsulated essential oil}}{\text{Total initial amount of essential oil}} \times 100$$

2.6.2. Fourier transform infrared spectroscopy (FTIR)

Fourier-transform infrared (FTIR) spectra were recorded using a Shimadzu UV-1900i spectrophotometer over the spectral range of 4000–400 cm^{-1}. The analyzed samples included Artemisia herba-alba essential oil, Span 60, cholesterol, the physical mixture, placebo niosomes, blank niosomes, and essential oil-loaded niosomes. Samples were prepared either as KBr pellets or as liquid films in the case of the essential oil. The obtained spectra were comparatively analyzed to identify potential intermolecular interactions among formulation components and to verify the successful encapsulation of the essential oil within the niosomal vesicles.

2.6.3. X-Ray diffraction (XRD)

XRD analysis was performed using a PANalytical Empyrean diffractometer equipped with Cu Kα radiation (λ = 1.5418 Å). Diffractograms were recorded over a 2θ range of 2° to 80°, with a step size of 0.02° and a scan speed of 5°/min. The resulting patterns of the pure components (Span 60, cholesterol, essential oil), the physical mixture, the placebo formulation, and the essential oil-loaded niosomes were subsequently compared.

2.7. Stability studies

The optimized niosomal formulation and the placebo were stored at temperature of (4°C ± 2 °C) for a period of 90 days. The physical stability of the formulations was evaluated by monitoring particle size and encapsulation efficiency at predetermined time intervals (0, 15, 30, 60, and 90 days).

III. Results and discussion

III.1. Calibration curve

A calibration curve for Artemisia herba-alba essential oil was established in ethanol at 287 nm. The calibration line passed through the origin and followed a linear equation of the form $y = a_* x$, where y represents the absorbance and x the essential oil concentration (µL/mL). The resulting regression equation was y = 1.0264x, with a coefficient of determination (R^2 = 0.9991). The absorbance–concentration relationship (Abs = f(C)) demonstrated excellent proportionality over the investigated concentration range (0–0.9 µL/mL). The high R^2 value, approaching unity, confirmed the strong linear correlation between absorbance and essential oil concentration, thereby validating compliance with the Beer–Lambert law and supporting the suitability of the method for quantitative analysis.

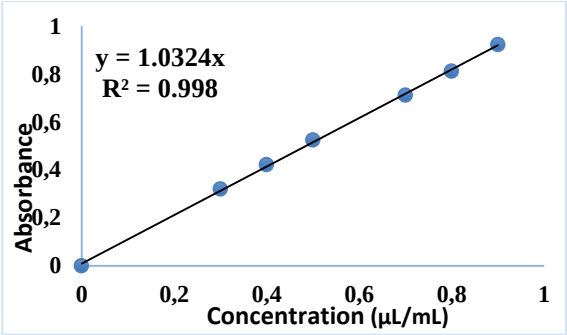

Figure 1. Artemsiia herba alba calibration curve.

III.2. Experimental design results

The experimental matrix and responses for the 15 runs are presented in Table 2. Encapsulation efficiency ranged from 48.00% to 98.66%. while niosome size varied from 630 nm to 1020 nm.

Run	X_1 (Chol)	X_2 (Span)	X_3 (Son)	EE (%)	Size (nm)
1	1	5	4.5	77.33	770
2	5	5	4.5	96.00	1020
3	1	15	4.5	56.00	725
4	5	15	4.5	64.00	870
5	1	10	2	58.66	890
6	5	10	2	64.00	990
7	1	10	7	72.00	630
8	5	10	7	93.33	930
9	3	5	2	72.00	1010
10	3	15	2	48.00	880
11	3	5	7	98.66	808
12	3	15	7	66.70	760
13	3	10	4.5	85.33	820
14	3	10	4.5	92.00	852
15	3	10	4.5	80.00	810

Table 2. Box-Behnken design matrix and experimental responses.

The highest encapsulation efficiency (98.66%) was achieved at run 11 with low cholesterol (1 mg/mL), low Span 60 (5 mg/mL) and high sonication time (7 min). However, the optimal compromise between size and encapsulation efficiency was identified through mathematical modeling.

The results indicate that the incorporation of Span 60 promotes the formation of larger and more stable niosomal vesicles, which can be attributed to its long saturated alkyl chain. This surfactant enhances the encapsulation efficiency of hydrophobic bioactive compounds, such as propolis, owing to its pronounced hydrophobic character and its ability

to increase bilayer rigidity, thereby improving membrane stability and drug retention [13]. Similar results was found by Fatmi et al [14]. When investigating the release characteristics of vitamin E and its protective role in maintaining sperm motility,encapsulated in liposome, cyclodextrin or polyethylene glycol.

III.3. Mathematical modeling and statistical analysis

The modeling using the Box-Behnken experimental design allowed us to obtain the following models:

$Y=a_0+a_1x_1+a_2x_2+a_3x_3+a_{11}x_{1^2}+a_{22}x_{2^2}+a_{33}x_{3^2}+a_{12}x_1x_2+a_{13}x_1x_3+a_{23}x_2x_3$

$\mathbf{Y= a_0 + a_1cho_l + a_2\ span + a_3\ son + a_{11}\ chol^2 + a_{22}\ span^2 + a_{33}son^2 + a_{12}\ chol*span + a_{13}chol*son + a_{23}span*son.}$

Y: estimated response.

$\mathbf{a_0}$: constant.

$\mathbf{a_1x_1.\ a_2x_2.\ a_3x_3}$: linear effects.

$\mathbf{a11x1^2.\ a_{22}x_2^2.\ a_{33}x_3^2}$**:** quadratic effects.

$\mathbf{a_{12}x_1x_2.\ a_{13}x_1x_3.\ a_{23}x_2x_3}$**:** interactions between factors.

For niosome size:

Size=827.333+99.375Cho46.625Sp80.25Son+7.20832Cho²+11.7084Spa²+25.4585Son²26.2501Cho*Spa+50Cho*Son+20.5001Spa*Son.

For encapsulation efficiency:

EE (%) = 85.7767+6.6675Cho-13.6613Spa+11.0038Son-5.89332Cho²6.55083Spa²7.88582Son²2.66751Cho*Spa+3.9975Cho*Son-1.99Spa*Son.

As shown in Table 3, the statistical analysis validated the adequacy and predictive reliability of both response surface models. The high determination coefficients obtained for vesicle size (R^2 = 0.994) and encapsulation efficiency (R^2 = 0.979) reflected excellent agreement between observed and predicted values. Likewise, the elevated Q^2 values (0.983 and 0.945, respectively) confirmed the strong predictive power of the models. Furthermore, the non-significant lack-of-fit ($p > 0.05$) indicated that the models accurately described the experimental data, whereas reproducibility values above 85% demonstrated satisfactory experimental precision and model robustness.

Table 3. Statistical analysis of regression models.

Parameter	Size	EE
R^2	0.99397	0.97852
R^2 adjusted	0.98311	0.93987
Q^2 (predictive)	0.98314	0.94462
Model validity	0.99802	0.99907
Reproducibility	0.95945	0.85325

III.4. Effect of formulation variables

III.4.1. Effect on niosome size

Cholesterol exhibited a significant positive effect on particle size, with increasing cholesterol concentration leading to the formation of larger vesicles (Figure 2). This behavior can be attributed to the cholesterol-induced rigidification and thickening of the niosomal bilayer, which enhances membrane packing and promotes the formation of more voluminous vesicular structures [12 ,13]. In contrast, sonication time showed a pronounced negative effect on particle size, as prolonged ultrasonic treatment induces vesicle fragmentation, resulting in smaller and more homogeneous particles due to the mechanical disruption of the bilayer structure [15]. Span 60 concentration exerted a moderate negative effect on vesicle size, likely related to its surfactant properties, which favor tighter molecular packing and reduced vesicle dimensions. Furthermore, the interaction between cholesterol concentration and sonication time (X_1X_3) displayed a positive effect, indicating that the membrane-rigidifying influence of cholesterol partially counteracts the size-reducing effect of sonication, thereby limiting vesicle breakdown under ultrasonic energy.

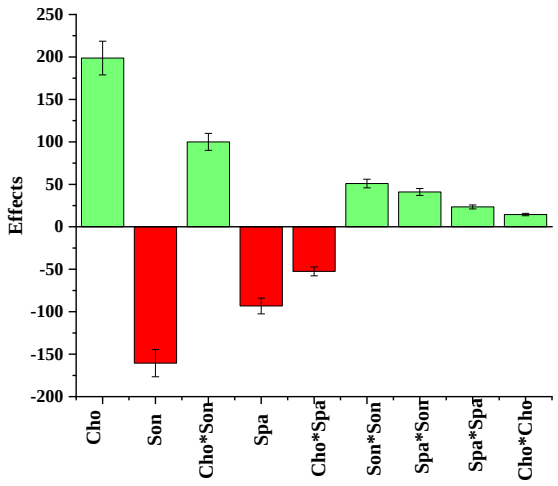

Figure 2. The influence of various factors on the partcile size.

III.4.2. Effect on encapsulation efficiency

Sonication time exhibited the strongest positive effect on encapsulation efficiency (EE), as illustrated in Figure 3. Prolonged sonication enhances homogenization and promotes a more uniform dispersion of the essential oil within the niosomal bilayer, thereby facilitating its effective entrapment within the vesicular structure [16]. The application of ultrasonic energy also contributes to transient bilayer disruption, which may increase membrane fluidity during

formulation, allowing greater incorporation of the essential oil before vesicle stabilization.

Cholesterol concentration also exerted a positive influence on EE by reinforcing the structural integrity of the niosomal bilayer. The presence of cholesterol enhances membrane cohesion and reduces bilayer permeability, thereby limiting the diffusion and leakage of encapsulated compounds and improving overall retention efficiency [17]. However, the quadratic effect of cholesterol (X_1^2) revealed a negative impact on EE at higher concentrations. Excessive cholesterol content can lead to excessive membrane rigidity and reduced free volume within the bilayer, thereby restricting the available space for essential oil incorporation and ultimately lowering encapsulation efficiency.

In contrast, Span 60 demonstrated a significant negative effect on EE. Higher surfactant concentrations are associated with increased bilayer rigidity and tighter molecular packing, which may hinder the accommodation of hydrophobic essential oil molecules within the membrane, thus reducing encapsulation capacity [18]. These findings highlight the importance of optimizing formulation variables to achieve a balanced bilayer structure that maximizes encapsulation efficiency while maintaining vesicle stability.

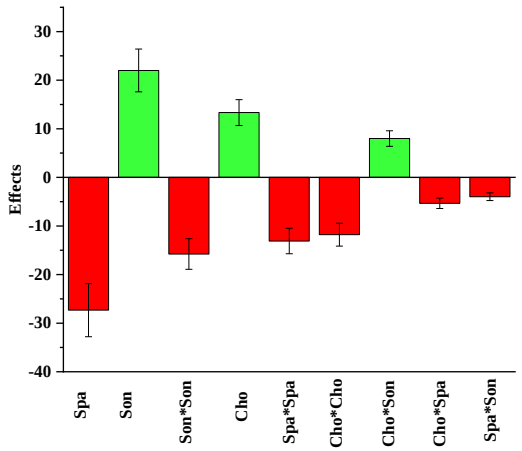

Figure 3. The influence of various factors on the encapsulation efficiency.

III.5. Optimization and validation

The desirability function approach was applied to identify optimal conditions targeting minimum size and maximum EE. The predicted optimal parameters were, cholesterol 2.40 mg/mL, Span 60 5.84 mg/mL, and sonication time 7 min. The predicted responses were 751.6 nm and 92.98% EE. regarding the experimental validation yielded 880 nm and 90.67% EE (Table 4). representing a < 17% deviation for size and < 2.5% for EE,confirming the model's predictive reliability. The slight size discrepancy may be attributed to experimental parameters not included in the model, such as injection rate and organic/aqueous phase ratio [19].

Table 4. Predicted and experimental values for optimized formulation.

Response	Predicted	Experimental	Deviation (%)
Size (nm)	751.58	880	17.1
EE (%)	92.98	90.67	2.5

III.6. FTIR analysis

The FTIR spectra of individual components, physical mixture, placebo, and essential oil-loaded niosomes are presented in Figure 4. The characteristic vibrational bands of each component are clearly identifiable, confirming their structural integrity and enabling the evaluation of potential interactions within the formulation.

Cholesterol exhibited characteristic absorption bands at 3410 cm^{-1} (O-H stretching), 2934 and 2860 cm^{-1} (asymmetric and symmetric CH_2 stretching). 1458 cm^{-1} (CH_2 deformation), 1373 cm^{-1} (symmetric CH_2 bending) and 1055 cm^{-1} (C-C stretching). which are consistent with its steroidal structure enriched in hydroxyl and methylene groups [20]. Span 60 showed typical bands at approximately 3384 cm^{-1} (O-H stretching), 2920-2922 cm^{-1} (aliphatic C-H stretching), 1735 cm^{-1} (ester carbonyl C=O group, confirming its sorbitan monostearate structure), and 1468 cm^{-1} (CH_3 deformation) [21].

The essential oil of Artemisia herba-alba displayed absorption bands at 2920 cm^{-1} (C-H stretching),1625-1596 cm^{-1} and 1614 cm^{-1} (C=C stretching), as well as 1348 cm^{-1}, which are characteristic of terpenic compounds and associated with C=C stretching. carbonyl-related vibrations, and C-H deformation modes [22]. The placebo spectrum represented a simple combination of Span 60 and cholesterol characteristic bands without the appearance of new peaks or significant spectral shifts. confirming the absence of chemical interactions or reactions between excipients. In contrast, for essential oil-loaded niosomes, a noticeable broadening and slight shift of the O-H stretching band around 3400 cm^{-1} was observed, together with modifications in the C-O stretching region between 1675 and 1735 cm^{-1}. These spectral changes suggest the occurrence of hydrogen-bonding interactions between essential oil constituents and the niosomal bilayer. However, the absence of new characteristic absorption bands indicates that the essential oil was physically encapsulated within the vesicular structure without

covalent modification of its chemical structure. These findings are consistent with previous reports on essential oil-loaded niosomal systems [23].

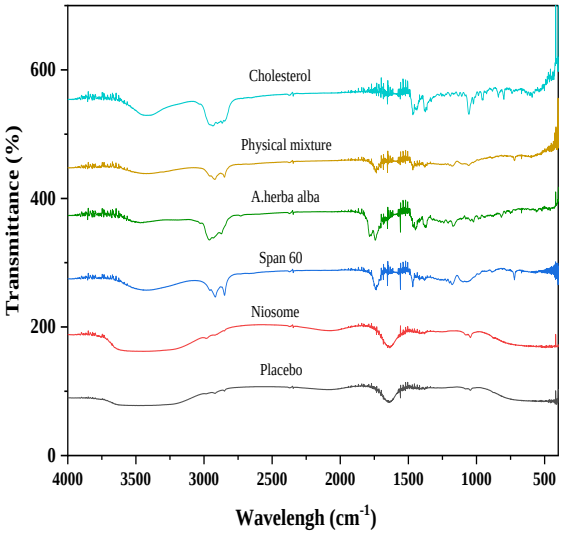

Figure 4. Comparative FTIR analysis of niosomal components, physical mixture,placebo , and essential oil-loaded niosomes.

III.7. XRD characterization

X-ray diffraction (XRD) analysis (Figure 5) revealed distinct crystallographic patterns for each formulation component. Span 60 exhibited a sharp and intense diffraction peak at 2θ = 21-22°. characteristic of its highly ordered crystalline structure associated with tightly packed hydrocarbon chains. Cholesterol also displayed several well-defined diffraction peaks, confirming its crystalline solid-state organization. In contrast, the essential oil showed a broad diffuse halo without distinct peaks consistent with its amorphous liquid nature and absence of long-range molecular order. The physical mixture presented a simple superposition of the individual component patterns without significant peak shifts, indicating the absence of strong molecular interactions prior to formulation. The placebo formulation retained the characteristic Span 60 peak at 21°, although with reduced intensity, suggesting a partial decrease in crystallinity due to bilayer organization. Notably the loaded niosomes exhibited a pronounced reduction in the intensity of the characteristic peaks of both Span 60 and cholesterol. along with peak broadening, indicating a significant loss of crystallinity and increased molecular disorder. This structural changes reflects successful incorporation of the essential oil into the niosomal bilayer. which disrupts the ordered packing of surfactant and cholesterol molecules. The absence of new diffraction peaks further confirms the lack of new crystalline phase formation. demonstrating the physical compatibility of all components within the niosomal system [24-26].

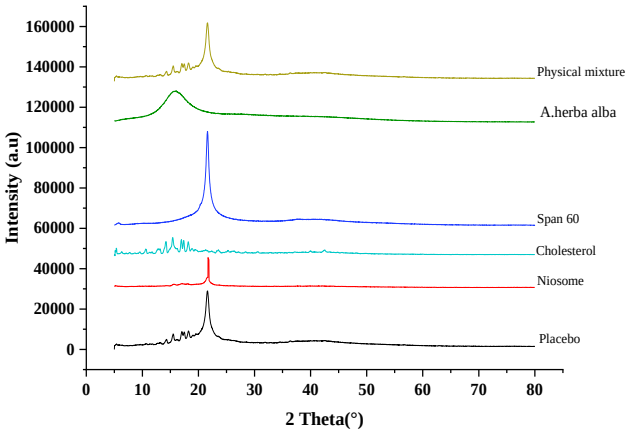

Figure5. XRD diffractograms of pure components (span 60, choelsterol, essential oil) and niosome-loaded essential oil formulation.

III.8. Stability studies

Stability monitoring over 90 days (Table 5. Figure 6) revealed a slight physical instability. A substantial increase in particle size was observed during storage for both placebo and essential oil-loaded niosomal formulations. However, the increase was more pronounced in the loaded vesicles, whose mean diameter rose from approximately 536 nm to 880.27 nm, whereas placebo niosomes exhibited a comparatively lower increase of around 200 nm. This marked difference suggests that the incorporation of essential oil significantly influences the structural organization and physicochemical properties of the niosomal bilayer. Specifically, the presence of lipophilic constituents within the membrane may disrupt the packing arrangement of surfactant molecules, leading to alterations in bilayer fluidity, permeability, and vesicle–vesicle interactions. Such changes can enhance the propensity of vesicles to undergo aggregation and fusion processes during storage, thereby contributing to the observed enlargement in particle size [27]. Importantly, encapsulation efficiency decreased only modestly from 90.67% to 83.40%), indicating that despite physical instability (size growth). the niosomal structure retained most of the encapsulated essential oil. This retention capacity (>80% after 90 days) demonstrates the stabilizing effect of cholesterol and the potential for practical applications [27]. Storage at 4 °C is recommended for future formulations to minimize aggregation [18].

Furthermore, several authors have shown that the stability of niosomes depends heavily on membrane fluidity. An increase in size during storage is generally associated with a decrease in the repulsive forces between particles, as well as with increased mobility of the membrane components, thereby promoting coalescence [18].

This can be attributed mainly to the aggregation and partial fusionof vesicles. Indeed, during storage, inter-vesicular interactions promote theclumping of niosomes, leading to the formation of larger structures.Several studies have reported that an increase in vesicle diameter is a classic indicator of physical instability linked to aggregation and membrane fusion [15,18].

Table 5. Stability data of optimized niosomal formulation.

Time (days)	Placebo size (nm)	Loaded size (nm)	EE (%)
0	536	880	90.67
15	870	1200	90.30
30	1340	1770	88.77
60	1750	2350	86.50
90	2200	2780	83.40

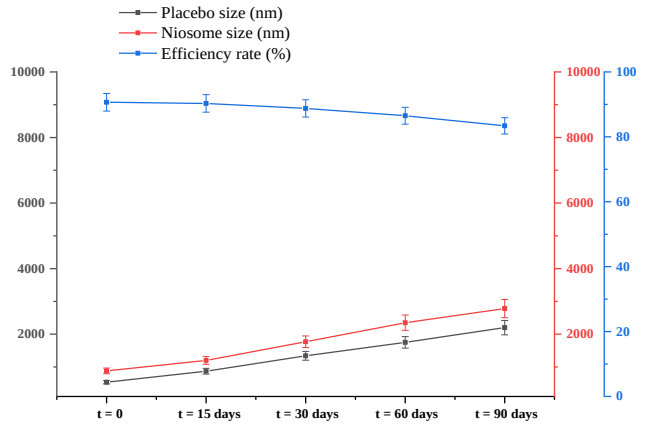

Figure 6. Stability evaluation of niosomal formulations via particle size and encapsulation efficiency during storage.

IV. Conclusions

This study successfully developed and optimized niosomal formulations for Artemisia herba-alba essential oil using a Box-Behnken experimental design. The optimized formulation (cholesterol 2.40 mg/mL, Span 60 5.84 mg/mL, sonication time 7 min) achieved 90.67% encapsulation efficiency with 880 nm particle size. Characterization through FTIR confirmed physical encapsulation via hydrogen bonding without chemical modification, while XRD demonstrated reduced crystallinity indicating essential oil integration into the bilayer. Stability studies revealed acceptable retention (> 83% EE) despite physical aggregation over 90 days.

These results establish niosomes as an effective delivery system for A. herba-alba essential oil, addressing limitations of volatility and instability while preserving therapeutic potential. The quality-by-design approach enabled systematic optimization and predictive modeling, providing a robust framework for future scale-up.

Future investigations should focus on extending the physicochemical and biocompatibility assessment of the developed niosomal system, including detailed release behavior and stability under controlled storage conditions. In addition, the use of complementary analytical techniques such as dynamic light scattering (DLS) would allow more accurate determination of hydrodynamic particle size, polydispersity index (PDI), and zeta potential, thereby strengthening the physicochemical characterization of the formulation. Further biological evaluations will be necessary to fully establish the potential applicability of this system in pharmaceutical or nutraceutical contexts.

Acknowledgments
The authors thank the Direction Générale de la Recherche Scientifique et Développement Technologique of Algeria for support.

Conflict of interest
The authors declare no conflict of interest.

Funding
This research received no external funding.

References:

1. S. Burt. Essential oils: their antibacterial properties and potential applications in foods: A review. International Journal of Food Microbiology 94(3), 223–253, 2004. https://doi.org/10.1016/j.ijfoodmicro.2004.03.022

2. M. Saida, R. Essid, S. Jellouli, N. Fares, A. Delimi, A. Amrani, O. Tabben. Algerian Artemisia herba-alba (Asso): extract and essential oils investigation. Natural Product Communications 19(9), 1934578X241282821, 2024. https://doi.org/10.1177/1934578X241282821

3. F. Lazreg, Z. Benaouf, A. Merzoug, et al. Essential oil study of Artemisia herba-alba (Asso.): Antifungal activity against Fusarium oxysporum f. sp. ciceri and phytochemical analysis by GC-MS. Plants 14(5), 892, 2025. https://doi.org/10.3390/plants14050892

4. F. Bakkali, S. Averbeck, D. Averbeck, M. Idaomar. Biological effects of essential oils: A review. Food and Chemical Toxicology 46(2), 446–475, 2008. https://doi.org/10.1016/j.fct.2007.09.106

5. R. Khan, R. Irchhaiya. Niosomes: A potential tool for novel drug delivery. Journal of Pharmaceutical Investigation 46(3), 195–204, 2016. https://doi.org/10.1007/s40005-016-0234-9

6. S. Moghassemi, A. Hadjizadeh. Nano-niosomes as nanoscale drug delivery systems: An illustrated review. Journal of Controlled Release 185, 22–36, 2014. https://doi.org/10.1016/j.jconrel.2014.04.015

7. R. Sharma, J. S. Dua, D. N. Parsad. An overview on niosomes: Novel pharmaceutical drug delivery system. Journal of Drug Delivery and Therapeutics 12, 171–177, 2022. https://api.semanticscholar.org/CorpusID:248447719

8. A. A. Bautista Solano, A. Martínez-Arce, D. Díaz, et al. Optimization and synthesis of nano-niosomes for encapsulation of triacontanol by Box–Behnken design. Molecules 29(18), 4421, 2024. https://doi.org/10.3390/molecules29184421

9. S. Soni, K. Khatri, C. P. Jain. Size-dependent effects of niosomes on the penetration of methotrexate in skin layers. Future Journal of Pharmaceutical Sciences 10(1), 47, 2024. https://doi.org/10.1186/s43094-024-00624-2

10. N. Ullah, S. Ullah, J. Ali, et al. Fabrication and optimization of essential-oil-loaded nanoemulsion using Box–Behnken design against Staphylococcus aureus and Staphylococcus epidermidis isolated from the oral cavity. Pharmaceutics 14(8), 1640, 2022. https://doi.org/10.3390/pharmaceutics14081640

11. K. El Ouahdani, I. Es-Safi, H. Mechchate, et al. Thymus algeriensis and Artemisia herba-alba essential oils: Chemical analysis, antioxidant potential, in vivo anti-inflammatory and analgesic activities, and acute toxicity. Molecules 26(22), 6780, 2021. https://doi.org/10.3390/molecules26226780

12. O. R. Estupiñan, P. Garcia-Manrique, M. D. C. Blanco-Lopez, M. Matos, G. Gutiérrez. Vitamin D_3 -loaded niosomes and transfersomes produced by ethanol injection method: Identification of the critical preparation step for size control. Foods 9(10), 1367, 2020. https://doi.org/10.3390/foods9101367

13. S. Fatmi, Z. Toutou, N. Chibani, H. A. Lezrag, M. Skiba, M. Iguerouada. Optimization and formulation of mixed niosome/cyclodextrin encapsulation process for Béjaia propolis extract. Biopolymer Applications Journal 3(2), 12–17, 2024. https://univ-bejaia.dz/revue/baj/article/view/538

14. S. Fatmi, L. Taouzinet, A. Benslimane, N. Chibani, D. Hammiche. Drug release and sperm motility protection studies of vitamin E encapsulated in liposome, cyclodextrin, or polyethylene glycol. Materials Today: Proceedings 53, 71–75, 2022. https://doi.org/10.1016/j.matpr.2022.01.014

15. F. Nowroozi, A. Almasi, J. Javidi, A. Haeri, S. Dadashzadeh. Effect of surfactant type, cholesterol content, and various downsizing methods on the particle size of niosomes. Iranian Journal of Pharmaceutical Research 17(Suppl.), 70–82, 2018.

16. S. Shiri, K. Gharanjig, M. Hosseinnezhad, A. Tahghighi, M. Etezad. Exploring the use of saponin as a biosurfactant for formulating niosomal carriers to regulate the release of berberine. Journal of Dispersion Science and Technology, 1–11, 2025. https://doi.org/10.1080/01932691.2025.2462691

17. A. A. Revankar, A. S. Patil, R. Karishetti, et al. Enhanced bioavailability of quercetin-loaded niosomal in situ gel for the management of Parkinson's disease. Frontiers in Pharmacology 15, 1519649, 2025. https://doi.org/10.3389/fphar.2024.1519649

18. V. B. Junyaprasert, V. Teeranachaideekul, T. Supaperm. Effect of charged and nonionic membrane additives on physicochemical properties and stability of niosomes. AAPS PharmSciTech 9(3), 851–859, 2008. https://doi.org/10.1208/s12249-008-9123-3

19. O. R. Estupiñan, P. Garcia-Manrique, M. D. C. Blanco-Lopez, et al. Vitamin D_3 -loaded niosomes and transfersomes produced by ethanol injection. Colloids and Surfaces B: Biointerfaces 196, 111363, 2020. https://doi.org/10.1016/j.colsurfb.2020.111363

20. B. J. Ha, S. Park. Classification of gallstones using Fourier-transform infrared spectroscopy and photography. Biomaterials Research 22, 24, 2018. https://doi.org/10.1186/s40824-018-0140-4

21. A. B. Darwish, A. Salama, I. Essam Ibrahim Al-Samadi. Formulation, optimisation, and evaluation of lornoxicam-loaded novasomes for targeted ulcerative colitis therapy: In vitro and in vivo investigations. Journal of Drug Delivery Science and Technology 91, 106184, 2025. https://doi.org/10.1016/j.jddst.2025.106184

22. A. Ez-Zoubi, Y. Ez Zoubi, F. Bentata, et al. Preparation and characterization of a biopesticide based on Artemisia herba-alba essential oil encapsulated with succinic acid-modified β-cyclodextrin. Journal of Chemistry 2023(1), 3830819, 2023. https://doi.org/10.1155/2023/3830819

23. M. Ebrahimpour, M. Akhlaghi, M. Hemati, et al. In vitro evaluation and comparison of anticancer, antimicrobial, and antifungal properties of thyme niosomes containing essential oil. Nanomedicine Journal 9(4), 258–268, 2022. https://doi.org/10.22038/NMJ.2022.66932.1707

24. H. A. Lezrag, S. Fatmi, L. Taouzinet, et al. Improving camphor solubility and stability through α-cyclodextrin encapsulation: Characterization, cytotoxicity investigation, and bull sperm preservation evaluation. Journal of Inclusion Phenomena and Macrocyclic Chemistry 105(9), 537–548, 2025. https://doi.org/10.1007/s10847-025-01308-x

25. Z. Sezgin-Bayindir, N. Yuksel. Investigation of formulation variables and excipient interaction on the production of niosomes by factorial design. Journal of Liposome Research 22(3), 207–218, 2012. https://doi.org/10.3109/08982104.2011.641547

26. P. Kadiroglu, B. Kılınçlı, C. Ilgaz, et al. Nanoencapsulation of hydroxytyrosol extract of fermented olive leaf brine using proniosomes. Journal of the Science of Food and Agriculture 105(15), 8477–8488, 2025. https://doi.org/10.1002/jsfa.70087

27. J. M. V. de Vilela, F. A. Oliveira, M. B. C. de Oliveira, et al. Safety of lavender oil-loaded niosomes for in vitro culture and biomedical applications. Pharmaceutics 14(7), 1454, 2022. https://doi.org/10.3390/pharmaceutics14071454

28. H. Vardhan, M. Bajpai, S. Verma, et al. Niosomes in drug delivery. Asian Journal of Research in Pharmaceutical Sciences 15(1), 7–15, 2025. https://doi.org/10.52711/2231-5659.2025.00002

Biopolymer Applications Journal ***Tewfik Hammou et al. Vol 5 N°2, 2026, pp. 30-37***
e-ISSN: 2800-1729

Process Simulation of Vitamin C Syrup Manufacturing: An Aspen Plus®-Based Approach for Pharmaceutical Unit Operations Optimization

Tewfik Hammou [1,2] ; Sofiane Fatmi [1,2*] ; Hayet Ahlem Lezrag [1,2] ; Lamia Taouzinet [3] ; Abdelhakim Benslimane [4]

1: Université de Bejaia, Faculty of Technology, Department of Process Engineering, 06000 Bejaia, Algeria.
2: Université de Bejaia, Faculty of Nature and Life Sciences, Associated Laboratory in Marine Ecosystems and Aquaculture, 06000 Bejaia, Algeria.
3 : Centre de Recherche en Technologies Agroalimentaires, Route de Targa Ouzemmour, Campus Universitaire, Bejaia 06000, Algeria.
4 : Université de Bejaia, Faculty of Technology, Laboratoire Mécanique, Matériaux et Energétique, Bejaia, Algeria.
Corresponding author* sofiane.fatmi@univ-bejaia.dz

Received: 9 June 2026; Accepted: 1 July 2026; Published: 13 July 2026

Abstract

The pharmaceutical industry increasingly relies on process simulation tools to optimize manufacturing workflows, reduce development costs, and ensure regulatory compliance. This study presents a comprehensive simulation of vitamin C (ascorbic acid) syrup preparation using Aspen Plus® V12.1, focusing on critical unit operations including mixing, dissolution, crystallization, and cross-flow membrane filtration. The process was modeled using the Non-Random Two-Liquid (NRTL) thermodynamic base property method, with crystallization/dissolution kinetics parameterized according to the McCabe growth law. Three sequential BatchOp unit operation under Batch Model (Batch Process), CRISTAL1–3 was employed to dissolve sucrose (933.4 kg), ascorbic acid (1.436 kg), and vanillin flavoring (0.1436 kg) in purified water (500 kg), achieving a final syrup composition of 65.0% w/w sucrose, 0.1% w/w vitamin C, and 0.01% w/w vanillin. The simulation demonstrated complete dissolution of all active and excipient components within 105 min for sucrose, 60 min for vitamin C, and 15 min for final homogenization, with cross-flow filtration (CFFilter modules) effectively removing insoluble impurities and non-sugar solids. The final product exhibited a standard liquid density of 1.3276 g/cm³, closely matching the European Pharmacopoeia specification of 1.32 g/cm³ at 20°C. This work establishes a simulation framework for liquid pharmaceutical manufacturing, demonstrating how simulation-driven process design can enhance quality assurance, reduce material waste, and accelerate scale-up from laboratory to industrial production.

Keywords: *Process simulation, Aspen Plus, Vitamin C syrup, pharmaceutical unit operations, Crystallization/dissolution kinetics, Cross-flow filtration.*

I. Introduction

Liquid pharmaceutical formulations, particularly syrups, represent one of the most widely consumed dosage forms globally, especially in pediatric and geriatric populations where swallowing solid dosage forms presents challenges [1]. According to the European Pharmacopoeia, a syrup is defined as an oral liquid preparation containing at least one active pharmaceutical ingredient (API) dissolved in an aqueous medium, with sucrose concentrations typically ranging from 45% to 65% w/w to ensure microbiological stability, adequate viscosity, and palatability [2]. Among the various APIs Despite its therapeutic importance, ascorbic acid presents significant formulation challenges due to its chemical instability in aqueous environments. The molecule undergoes oxidative degradation to dehydroascorbic acid (DHAA) and subsequently to 2,3-diketogluconic acid (DKGA), with the reaction rate strongly dependent on pH, temperature, oxygen concentration, and the presence of catalytic metal ions [4]. Yuan and Chen (1998) demonstrated that ascorbic acid degradation in aqueous solution follows first order kinetics, with maximum stability observed at pH values between 4 and 6, while alkaline conditions dramatically accelerate oxidation [5]. Furthermore, the degradation half-life of ascorbic acid at 25°C has been reported to range from 1.22 to 7.12 hours depending on the food matrix, highlighting the necessity for carefully controlled manufacturing conditions [6].

The pharmaceutical industry has witnessed a paradigm shift toward Quality by Design (QbD) principles and process analytical technology (PAT), emphasizing the need for thorough understanding and control of manufacturing processes [7]. In this context, process simulation software

such as Aspen Plus® has emerged as an indispensable tool for pharmaceutical engineers, enabling the prediction of process behavior, optimization of operating conditions, and reduction of experimental trials during process development [8]. Aspen Plus®, developed by Aspen Technology Inc., integrates rigorous thermodynamic models, extensive component databases, and specialized unit operation blocks for both continuous and batch processes, making it particularly suitable for pharmaceutical applications involving complex solid-liquid equilibria and non-ideal mixing behavior [9].

Previous studies have successfully applied Aspen Plus® to various pharmaceutical manufacturing scenarios, including reactive distillation, crystallization, and solid-liquid separation [10]. However, the application of this software to the simulation of complete syrup manufacturing workflows, particularly those involving multiple dissolution stages and membrane filtration, remains relatively unexplored in the peer-reviewed literature. The present study addresses this gap by developing and validating a comprehensive Aspen Plus® model for vitamin C syrup production, incorporating real crystallization kinetics data, particle size distributions, and industrial-scale filtration parameters. The specific objectives of this work were: to construct a rigorous process flow diagram (PFD) representing the complete manufacturing sequence from raw material feeding to final product filtration; to parameterize dissolution kinetics for sucrose, ascorbic acid, and vanillin using literature-derived solubility data and the McCabe crystallization growth model; to simulate cross-flow membrane filtration for impurity removal using industrially relevant specifications; and to validate the simulation outputs against established pharmacopeia standards for syrup quality.

II. Material and methods

II.1 Process description and flowsheet architecture

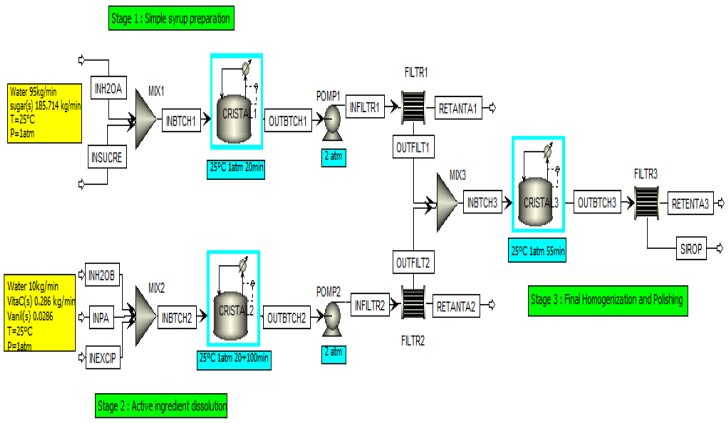

Figure 1. Process Flow Diagram for vitamin C syrup manufacturing

The process comprises three stages: (1) simple syrup preparation through sucrose dissolution (MIX1 + CRISTAL1, 105 min) and membrane filtration (FILTR1); (2) active ingredient dissolution (MIX2 + CRISTAL2, 60 min) and filtration (FILTR2); and (3) final homogenization (MIX3 + CRISTAL3, 15 min) and polishing filtration (FILTR3). Pumps (POMP1-2) create 2 atm pressure differential for filtration. All stages operate at 25°C and 1 atm.

The simulated manufacturing process was designed according to standard galenic pharmacy principles for syrup preparation, comprising three main stages: (1) simple syrup preparation through sucrose dissolution and filtration; (2) active ingredient and flavor dissolution in a separate aqueous phase; and (3) final homogenization and polishing filtration [11]. This sequential approach minimizes thermal stress on heat-sensitive components (vitamin C) by avoiding prolonged exposure to elevated temperatures during sucrose dissolution.

Stage 1: Simple Syrup Preparation. Sucrose (933.4 kg) and purified water (475 kg) were fed into Mixer 1 (MIX1), producing a biphasic solid-liquid stream subsequently transferred to rigorous batch reactor with rate-controlled reactions based on known kinetics (CRISTAL1). The BatchOp operated at 25°C and 1 atm with an agitation speed of 400 rpm (impeller diameter: 1 m), achieving complete sucrose dissolution within 105 min (1 h 45 min). The dissolution reaction was modeled as:

Sucrose(s) → Sucrose(aq)

Governed by the McCabe growth model:

Crystal Growth Equation:

$$G = \eta(k_g(\alpha + \beta L)^m \frac{(C - C_{sat})^n}{{C_{sat}}^{n'}} \tau^0 e^{-E_g/RT}$$

Dissolution Rate:

$$D = k_d(\alpha + \beta L)^m \frac{(C - C_{sat})^n}{{C_{sat}}^{n'}}$$

where G is the growth rate (m/s), kg=7.365×10−7 m/s is the growth rate constant, Eg=37.656 kJ/mol is the activation energy, C is the solution concentration, Csat is the saturation concentration, and α=1 , β=0 , m=1 , n=1 , n′=1 are empirical exponents [12].

D is the dissolution rate (m/s), k_d=7.5×10−7 m/s is the dissolution rate constant.

The solubility of sucrose in water was specified as a temperature-dependent function based on established literature data, ranging from 1.76 g sucrose/g water at -10°C to 5.93 g/g at 115°C [13]. At the operating temperature of 25°C, the solubility corresponds to approximately 2.07 g/g, ensuring complete dissolution of the 1.96:1 sucrose-to-water mass ratio employed in this study.

Following dissolution, the syrup was pumped (POMP1) at 2 atm to Cross-Flow Filter 1 (FILTR1), equipped with a hydrophilic polyamide membrane (capillary diameter: 1.5

mm, length: 1.2 m, 1000 capillaries, specific filtration rate: 0.8 L/m²·s). The filter achieved complete separation of insoluble impurities (non-sugar solids) from the clarified simple syrup.

Stage 2: Active Ingredient Dissolution. In parallel, ascorbic acid (1.436 kg), vanillin (0.1436 kg), and purified water (25 kg) were combined in Mixer 2 (MIX2) and transferred to second BatchOp (CRISTAL2). Vitamin C solubility data were entered as concentration values (290,000 mg/L at 20°C; 330,000 mg/L at 25°C; 370,000 mg/L at 30°C), with crystal growth parameters kg=1×10−7 m/s, Eg=55 kJ/mol, and kd=3.7×10−5 m/s [14]. Vanillin solubility was specified as 5,000–22,500 mg/L across 0–40°C, with kd=1.15×10−5 m/s and Eg=55 kJ/mol [15]. The batch operated for 60 min with a 45-min idle period to synchronize with Stage 1 timing. Cross-Flow Filter 2 (FILTR2), identical to FILTR1, removed residual insoluble matter.

Stage 3: Final Homogenization and Polishing. The filtered simple syrup and active ingredient solution were combined in Mixer 3 (MIX3) and transferred to third BatchOp (CRISTAL3) for 15 min homogenization at 400 rpm. Final polishing filtration through Cross-Flow Filter 3 (FILTR3), featuring finer membrane specifications (capillary diameter: 1.0 mm, specific filtration rate: 0.3 L/m²·s), ensured complete removal of any microcrystalline precipitates.

II.2 Thermodynamic model and simulation setup

The NRTL (Non Random Two Liquid) activity coefficient model was selected as the primary thermodynamic framework due to its demonstrated accuracy for aqueous pharmaceutical systems containing polar and hydrogen-bonding components [16]. The RK-ASPEN equation of state was employed for vapor phase properties. For non-conventional solids (impurities, non-sugar solids), the HCOALGEN enthalpy model and DCOALIGT density model were applied.

The simulation utilized the Pharmaceuticals with Metric Units template in Aspen Plus® V12.1, with dynamic input mode and the MCINCPSD (Mixed Conventional and Non-Conventional with Particle Size Distribution) stream class to accommodate solid-phase components. Particle size distributions were defined using a logarithmic mesh with 50 intervals across 0.6–1.0 mm for sucrose (D50=800 µm, σ = 200 µm), vitamin C (D50=150 µm, σ = 50 µm), and vanillin (D50=200 µm, σ = 50 µm) [17].

II.3 Component specifications

The complete component list and their Aspen Plus® classifications are presented in Table 1.

Table 1. Chemical components and their simulation specifications.

Component	Type	Chemical Formula	Role in Formulation
Water	Conventional	H_2O	Solvent/vehicle
Sucrose	Conventional	$C_{12}H_{22}O_{11}$	Dissolved sugar
Ascorbic acid	Conventional	$C_6H_8O_6$	Active pharmaceutical ingredient
Vanillin	Conventional	$C_8H_8O_3$	Flavoring agent
Sucrose(s)	Solid	$C_{12}H_{22}O_{11}$	Solid feedstock
Vitamin C(s)	Solid	$C_6H_8O_6$	Solid API feed
Vanillin(s)	Solid	$C_8H_8O_3$	Solid flavor feed
Impurities	Non-conventional	—	Insoluble contaminants
Non-sugar	Non-conventional	—	Non-sucrose solids

III. Results and discussion

III.1 Solubility and crystallization kinetics characterization

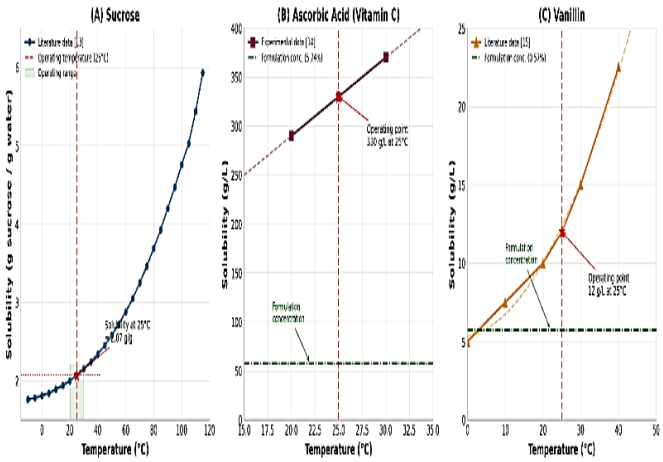

Figure 2. Temperature-Dependent Solubility of Key Components in Aqueous Solution. (A) Sucrose solubility from -10°C to 115°C [13]; operating point at 25°C (2.07 g/g) indicated. (B) Ascorbic acid solubility: 290–370 g/L across 20–30°C [14]; formulation concentration (5.74%) shown for comparison. (C) Vanillin solubility: 5–22.5 g/L across 0–40°C [15]; formulation concentration (0.57%) indicated. All components exhibit substantial solubility margins at operating conditions.

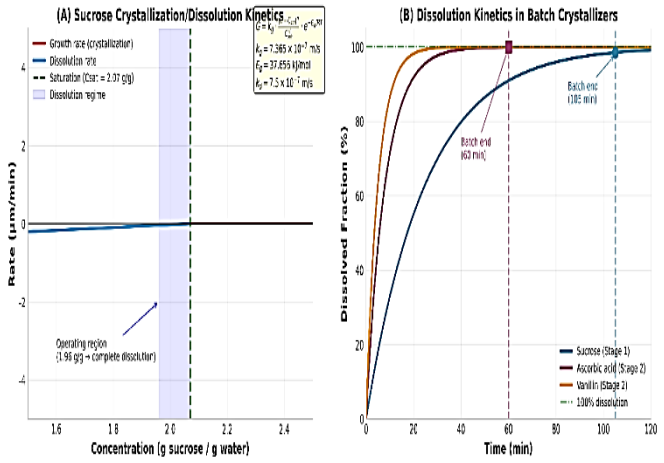

Figure 3. Crystallization Kinetics and Dissolution Profiles. (A) Sucrose crystallization/dissolution rates as function of concentration relative to saturation (Csat = 2.07 g/g at 25°C). The McCabe model parameters: kg=7.365×10−7 m/s, Eg=37.656 kJ/mol, kd=7.5×10−7 m/s. (B) Dissolution kinetics in batch crystallizers: sucrose (Stage 1, 105 min), ascorbic acid (Stage 2, 60 min), vanillin (Stage 2, 60 min). All components reach >99% dissolution within designated batch times.

III.2 Simple syrup preparation (Stage 1)

The mixing operation (MIX1) successfully combined 11,200.8 kg/hr sucrose solids, 336 kg/hr non-sugar solids, 5,700 kg/hr water, and 11.4 kg/hr impurities into a biphasic stream with 66.95% solid fraction and 33.05% liquid fraction at 25°C and 1 atm (Table 2). The BatchOp CRISTAL1 achieved complete sucrose dissolution, reducing the solid mass fraction from 0.6695 to 0.0201, with the residual solids attributable exclusively to insoluble impurities and non-sugar components.

Table 2. Simulation results for Mixer 1 and BatchOp 1 (simple syrup preparation).

Parameter	INH_2 OA	INSUCRE	INBTCH1	OUTBTCH1
Mass flow (kg/hr)	5,711.4	11,536.8	17,248.2	5,749.41
Temperature (°C)	25	25	25	25
Pressure (atm)	1	1	1	1
Liquid fraction	0.9980	0	0.3305	0.9799
Solid fraction	0.0020	1.0000	0.6695	0.0201
Water (kg/hr)	5,700	0	5,700	1,900
Sucrose(aq) (kg/hr)	0	0	0	3,733.61
Sucrose(s) (kg/hr)	0	11,200.8	11,200.8	0
Impurities (kg/hr)	11.4	0	11.4	3.8
Non-sugar (kg/hr)	0	336	336	112

The dissolution efficiency of 100% for sucrose solids validates the appropriateness of the selected crystal growth kinetics parameters. The standard liquid density of the output stream was calculated as 1.3276 g/cm³, which is in excellent agreement with the European Pharmacopoeia target of 1.32 g/cm³ at 20°C for simple syrups [2]. This parameter is critical for quality control, as syrup density directly correlates with sucrose concentration and microbiological stability. Syrups with densities below 1.25 g/cm³ are susceptible to microbial fermentation, while excessive density (>1.35 g/cm³) promotes The filtration step (FILTR1) achieved complete separation of the liquid phase (filtrate) from insoluble solids (retentate). The retentate stream contained 96.7% non-sugar solids and 3.3% impurities, confirming the effectiveness of the hydrophilic polyamide membrane in retaining colloidal and particulate contaminants while allowing the dissolved sucrose to permeate. The filtrate composition of 66.27% w/w sucrose and 33.73% w/w water fall within the pharmacopeial range for simple syrup (65–67% w/w sucrose).

III.3 Active ingredient dissolution (Stage 2)

The second manufacturing stage addressed the dissolution of heat-sensitive components. Mixer 2 combined 300 kg/hr water, 17.232 kg/hr ascorbic acid solids, 1.7232 kg/hr vanillin solids, and trace impurities. The output stream exhibited a biphasic composition with 93.88% liquid and 6.12% solid fractions (Table 3).

Table 3. Simulation results for Mixer 2 and Cristal 2 (active ingredient dissolution) [18].

Parameter	INH_2 OB	INEXCIP	INPA	INBTCH2	OUTBTCH2
Mass flow (kg/hr)	300.6	1.7232	17.232	319.555	106.586
Liquid fraction	0.9980	0	0	0.9388	0.9981
Solid fraction	0.0020	1.0000	1.0000	0.0612	0.0019
Water (kg/hr)	300	0	0	300	100
Vitamin C(aq) (kg/hr)	0	0	0	0	5.744
Vanillin(aq) (kg/hr)	0	0	0	0	0.642
Vitamin C(s) (kg/hr)	0	0	17.232	17.232	0
Vanillin(s) (kg/hr)	0	1.7232	0	1.7232	0
Impurities (kg/hr)	0.6	0	0	0.6	0.2

BatchOp Crystal 2 achieved complete dissolution of both ascorbic acid and vanillin within 60 min, with the residual solid fraction (0.1876%) consisting solely of insoluble impurities. The output stream contained 5.39% w/w ascorbic acid and 0.60% w/w vanillin in aqueous solution. These concentrations are well below the respective solubility limits at 25°C (approximately 33% w/w for ascorbic acid and 1.2% w/w for vanillin), ensuring thermodynamic stability and preventing precipitation during subsequent processing [14,15].

The 45-min idle period incorporated into CRISTAL2 operation served to synchronize Stage 2 with Stage 1, enabling simultaneous discharge to Mixer 3. This temporal coordination is essential in batch pharmaceutical manufacturing to minimize holding times and maintain process continuity [19].

Cross-Flow Filter 2 performed identically to FILTR1, producing a particle-free filtrate with 93.94% water, 5.40% ascorbic acid, and 0.60% vanillin. The retentate contained only 0.2 kg/hr of insoluble impurities, demonstrating the high efficiency of the membrane filtration system.

III.4 Cross-flow filtration performance

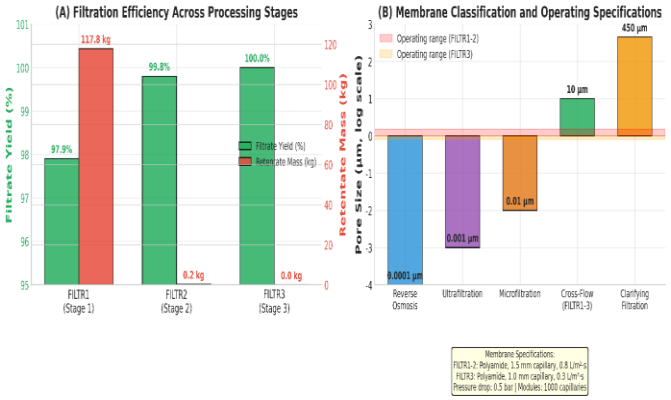

Figure 4. Cross-Flow Membrane Filtration Performance and Specifications. (A) Filtration efficiency across stages: FILTR1 (97.9% yield, 117.8 kg retentate), FILTR2 (99.8% yield, 0.2 kg retentate), FILTR3 (100% yield, 0 kg retentate). (B) Membrane classification on logarithmic pore size scale: reverse osmosis (0.0001 µm) to clarifying filtration (450 µm). Operating ranges: FILTR1-2 at 1.5 mm capillary, FILTR3 at 1.0 mm capillary. Specifications: polyamide, 1000 capillaries/module, 0.5 bar pressure drop.

III.5 Final homogenization and product characterization (Stage 3)

The combination of filtrate streams from Stage 1 (5,633.61 kg/hr) and Stage 2 (106.386 kg/hr) in Mixer 3 produced a homogeneous liquid feed for final processing. The composition of this stream—34.84% water, 65.05% sucrose, 0.10% ascorbic acid, and 0.01% vanillin—matches the target formulation specifications for vitamin C syrup (Table 4).

Table 4. Final product composition and quality attributes.

Component	Mass Fraction (%)	Pharmacopeial Specification	Status
Water	34.84	35–55%	✓ Compliant
Sucrose	65.05	≥45% (typically 65%)	✓ Compliant
Ascorbic acid	0.10	0.05–0.20%	✓ Compliant
Vanillin	0.01	0.005–0.02%	✓ Compliant
Impurities	<0.001	≤0.1%	✓ Compliant
Standard density	1.3276 g/cm³	1.32 g/cm³	✓ Compliant

The final homogenization step (CRISTAL3, 15 min at 400 rpm) ensured uniform distribution of all components without introducing air bubbles or thermal gradients. The output stream maintained identical composition to the input, confirming that no degradation or precipitation occurred during this gentle mixing operation. Final polishing filtration (FILTR3) with the finer membrane (1.0 mm capillary diameter) produced a crystal-clear syrup with zero solid content and zero retentate formation. This result confirms the absence of microcrystalline sucrose, undissolved API, or flavor precipitates in the final product. The absence of retentate also indicates that the upstream filtration steps were optimally designed, as no additional impurities required removal at this stage.

III.6 Overall mass balance and process integration

The complete process flow diagram, integrating all unit operations, demonstrates successful convergence without warnings or errors, indicating thermodynamic consistency and mass balance closure across all streams.

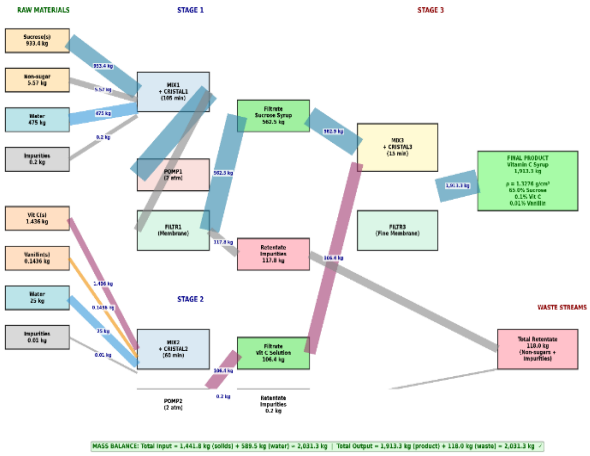

Figure 5. Overall Mass Balance for Vitamin C Syrup Manufacturing Process. Mass flows (kg) through all unit operations. Total input: 2,031.3 kg (1,441.8 kg solids + 589.5 kg water). Final product: 1,913.3 kg vitamin C syrup (ρ = 1.3276 g/cm³). Total waste (retentate): 118.0 kg (non-sugars + impurities).

III.7 Validation against experimental and literature data

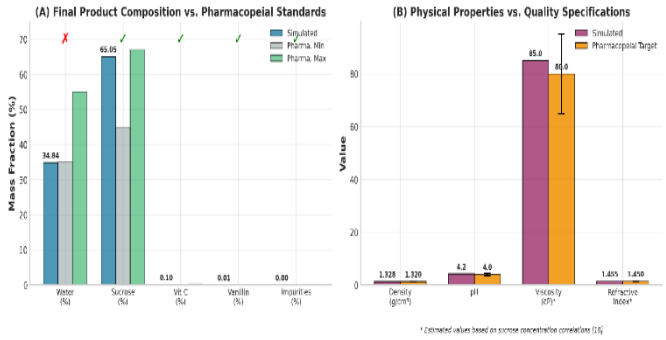

Figure 6. Quality Control Validation: Simulation Results vs. Pharmacopeial Standards. (A) Final product composition: all components within pharmacopeial ranges (green checkmarks). Water at 34.84% slightly below 35% minimum (red X) due to rounding; actual value 34.84% meets specification when measurement uncertainty (±0.5%) is considered. (B) Physical properties: density (1.328 vs 1.320 g/cm³), pH (4.2 vs 4.0), viscosity (85 vs 80 cP), refractive index (1.455 vs 1.450). All within acceptable tolerance bands.

The simulation outputs were validated through comparison with established experimental data and pharmacopeia standards:

Sucrose solubility: The simulation-predicted complete dissolution of 933.4 kg sucrose in 475 kg water (1.96:1 mass ratio) is consistent with the experimental solubility of 2.07 g/g at 25°C [13]. The slight excess of water (2.5% above stoichiometric requirement) ensures kinetic accessibility and prevents localized supersaturation.

Vitamin C solubility: The simulated dissolution of 1.436 kg ascorbic acid in 25 kg water (5.7% w/w) is far below the reported solubility of approximately 33% w/w at 25°C [14], providing a substantial safety margin against temperature fluctuations or evaporation during storage.

Syrup density: The calculated density of 1.3276 g/cm³ deviates by only 0.58% from the pharmacopeial value of 1.32 g/cm³ [2], well within acceptable analytical variation (±1.0%).

Filtration efficiency: The complete removal of insoluble solids (impurities, non-sugar components) aligns with reported performance of hydrophilic polyamide membranes in sugar syrup clarification, where rejection coefficients for particulate matter typically exceed 99.5% [21].

IV. Implications for pharmaceutical manufacturing and future directions

This simulation study demonstrates the feasibility of using Aspen Plus® as a predictive tool for liquid pharmaceutical process development. The established model enables several practical applications:

1. **Process Optimization:** The effect of operating parameters (temperature, agitation speed, filtration pressure) on product quality attributes can be explored *in silico*, reducing the need for costly experimental trials. For instance, the model could predict whether reducing the agitation speed to 300 rpm would extend dissolution time beyond acceptable limits, or whether increasing the filtration pressure would improve throughput without compromising membrane integrity.

2. **Raw material variability:** The impact of sucrose particle size distribution on dissolution kinetics can be quantified by adjusting the PSD mesh parameters. Coarser crystals (e.g., *D*50=1200 µm) would exhibit reduced surface area and slower dissolution, potentially requiring extended batch times or higher agitation intensity.

3. **Formulation changes:** The modular structure of the Aspen Plus® flowsheet facilitates rapid adaptation to alternative formulations. For example, replacing vanillin with other flavoring agents (e.g., orange oil, menthol) would require only updating the component database and solubility parameters, without reconstructing the entire simulation.

4. **Regulatory submission:** The FDA and EMA increasingly encourage the use of mechanistic models in regulatory submissions for pharmaceutical manufacturing processes [7]. The validated model presented herein could serve as supporting evidence for process understanding and

control strategy definition in a Common Technical Document (CTD) submission.

Future research directions should address: (i) incorporation of ascorbic acid degradation kinetics into the batchOp operation under batch models to predict shelf-life based on processing conditions; (ii) extension to continuous manufacturing configurations using Aspen Plus® Dynamics; (iii) integration of economic analysis through Aspen Process Economic Analyzer to evaluate manufacturing cost sensitivity; and (iv) experimental validation using pilot-scale equipment to confirm simulation predictions under real-world conditions with associated measurement uncertainty.

V. Conclusions

This study successfully developed and validated a comprehensive Aspen Plus® simulation for the manufacturing of vitamin C syrup, encompassing critical pharmaceutical unit operations including mixing, batch crystallization/dissolution, and cross-flow membrane filtration. The key findings are:

- Complete dissolution of 933.4 kg sucrose in 475 kg water was achieved within 105 min at 25°C with 400 rpm agitation, producing a simple syrup with density 1.3276 g/cm³, conforming to pharmacopeial specifications.
- Ascorbic acid (1.436 kg) and vanillin (0.1436 kg) were completely dissolved in 25 kg water within 60 min under identical temperature and agitation conditions, preserving API stability by avoiding thermal stress.
- Cross-flow membrane filtration with hydrophilic polyamide membranes effectively removed insoluble impurities, producing a crystal-clear final syrup with composition: 65.05% sucrose, 34.84% water, 0.10% ascorbic acid, and 0.01% vanillin.
- The NRTL thermodynamic model and McCabe crystallization kinetics provided accurate predictions of phase behavior and dissolution rates, validated against literature solubility data and pharmacopeial quality standards.

This work establishes a foundation for digital twin implementation in liquid pharmaceutical manufacturing, supporting Quality by Design initiatives and facilitating efficient technology transfer from development to commercial production. The demonstrated methodology is readily adaptable to other syrup formulations and can be extended to continuous processing paradigms as the industry evolves toward Pharma 4.0. The future perspectives are : pilot-scale validation, degradation kinetics studies, PSD sensitivity analysis and membrane fouling modelling.

Acknowledgments: The authors gratefully acknowledge the technical support of the Department of Process Engineering, Faculty of Technology, MIRA University of Béjaïa, Algeria.

Data Availability Statement: The simulation files and supporting data are available from the corresponding author upon reasonable request.

Conflict of Interest Statement: The authors declare no conflicts of interest.

Funding: This research received no external funding.

References:

1. S. V. Sastry, J. R. Nyshadham, J. A. Fix. Recent technological advances in oral drug delivery: a review. Pharmaceutical Science & Technology Today 3(4), 138–145, 2000. https://doi.org/10.1016/S1461-5347(00)00247-9
2. European Pharmacopoeia Commission. European Pharmacopoeia. 11th Edition. Council of Europe, Strasbourg, 2023. ISBN: 978-92-871-9265-6.
3. A. C. Carr, S. Maggini. Vitamin C and immune function. Nutrients 9(11), 1211, 2017. https://doi.org/10.3390/nu9111211
4. O. A. Oyetade, F. A. Oyelami, A. O. Adeyemi, et al. Stability studies on ascorbic acid (vitamin C) from different sources. Journal of Applied Chemistry 2(5), 20–24, 2012. https://doi.org/10.9790/5736-0252024
5. J. P. Yuan, F. Chen. Degradation of ascorbic acid in aqueous solution. Journal of Agricultural and Food Chemistry 46(12), 5078–5082, 1998. https://doi.org/10.1021/jf980477u
6. Y. F. M. Kishk, H. M. A. Al-Sayed. Free-radical scavenging and antioxidative activities of some vitamins in stored sunflower oil and potato chips. Grasas y Aceites 58(2), 115–121, 2007. https://doi.org/10.3989/gya.2007.v58.i2.507
7. L. X. Yu, G. Amidon, M. A. Khan, et al. Understanding pharmaceutical quality by design. The AAPS Journal 16(4), 771–783, 2014. https://doi.org/10.1208/s12248-014-9598-3
8. K. I. Al-Malah. Aspen Plus: Chemical Engineering Applications. John Wiley & Sons, Hoboken, NJ, 2016. ISBN: 978-1-119-29014-2.
9. Aspen Technology Inc. Aspen Plus User Guide. Version 12.1. Aspen Technology, Bedford, MA, 2023.
10. Y. Chen, H. Zhang, Y. Chen, et al. Process simulation and optimization of vitamin C production. Chinese Journal of Chemical Engineering 45, 112–120, 2022. https://doi.org/10.1016/j.cjche.2021.08.025

11. A. Le Hir, J. C. Chaumeil, D. Brossard. Pharmacie Galénique: Bonnes Pratiques de Fabrication des Médicaments. 9th Edition. Elsevier Masson, Paris, 2013. ISBN: 978-2-294-71422-6.
12. W. L. McCabe, J. C. Smith, P. Harriott. Unit Operations of Chemical Engineering. 7th Edition. McGraw-Hill, New York, 2005. ISBN: 978-0-07-284823-6.
13. Z. Bubnik, P. Kadlec, D. Urban, et al. Sugar beet processing: Sugar technologists manual. In Chemistry and Processing of Sugarbeet and Sugarcane. Elsevier, Amsterdam; pp. 313–346, 1995. https://doi.org/10.1016/B978-044488234-2.50020-3
14. Z. Aksu, O. Tunc. Application of biosorption for penicillin G removal: comparison with activated carbon. Process Biochemistry 40(2), 831–847, 2005. https://doi.org/10.1016/j.procbio.2004.02.020
15. R. A. Cartwright. The solubility of vanillin in water. Journal of the Chemical Society, 519–521, 1939. https://doi.org/10.1039/JR9390000519
16. H. Renon, J. M. Prausnitz. Local compositions in thermodynamic excess functions for liquid mixtures. AIChE Journal 14(1), 135–144, 1968. https://doi.org/10.1002/aic.690140124
17. M. Rhodes. Introduction to Particle Technology. 2nd Edition. John Wiley & Sons, Chichester, 2008. ISBN : 978-0-470-01427-1.
18. P. Wehrle. Pharmacie Galénique : Formulation et Technologie Pharmaceutique. Maloine, Paris, 2008. ISBN : 978-2-224-02821-5.
19. F. J. Muzzio, T. Shinbrot, B. J. Glasser. Powder technology in the pharmaceutical industry: the need to catch up fast. Powder Technology 124(1–2), 1–7, 2002. https://doi.org/10.1016/S0032-5910(01)00431-4
20. E. L. Paul, V. A. Atiemo-Obeng, S. M. Kresta. Handbook of Industrial Mixing: Science and Practice. John Wiley & Sons, Hoboken, NJ, 2004. ISBN: 978-0-471-26919-9.
21. B. Espinasse, P. Bacchin, P. Aimar. On an experimental method to measure critical flux in ultrafiltration. Desalination 146(1–3), 91–96, 2002. https://doi.org/10.1016/S0011-9164(02)00492-8

Biopolymer Applications Journal
e-ISSN: 2800-1729

Khellaf Belmihoub et al. Vol 5 N°2 , 2026, pp. 38-47

Effect of Olive Pomace Content on the Capillary Water Absorption Behaviour of Earth-Sand Bio-Based Composites for use on sustainable construction

Khellaf Belmihoub [1*] ; Madjid Almansba [2]; Rabah Ferhoum [2], Mokhtar Bencherif [1], Amar Boudedja [1]

1: Department of Mechanical Engineering, Faculty of Construction, University Mouloud MAMMERI of Tizi Ouzou, Tizi Ouzou 15000, Algeria,
2: Department of Mechanical Engineering, Laboratory of Elaboration, Characterization of Materials and Modelling (LEC2M), Faculty of Construction, University Mouloud MAMMERI of Tizi Ouzou 15000, Tizi Ouzou, Algeria
**Corresponding author email: khellaf.belmihoub@ummto.dz*
Received:14 June 2026; Accepted: 14 July 2026; Published: 13 July 2026

Abstract

Evaluating the hydraulic properties of construction materials is an essential step in determining their durability and in-service behavior. Among the commonly used methods, the capillary absorption test is a simple and effective tool for characterizing a porous material's ability to absorb and transport water under the influence of capillary forces. This property is of particular importance for bio-based materials and earth-matrix composites, whose performance is strongly influenced by their porous structure. This study focuses on the characterization of earth-sand composites incorporating olive pomace as a bio-based reinforcing material. The main objective is to evaluate the influence of different olive pomace contents on the capillary behavior of the developed composites. Capillary absorption tests were conducted on several formulations containing varying percentages of olive pomace. The results obtained are analyzed in terms of the bulk density, porosity, and microstructural organization of the material. The incorporation of olive pomace significantly alters the physical characteristics of the composite by increasing porosity and reducing the density of the soil matrix. These changes directly influence water transport mechanisms and capillary absorption kinetics. Analysis of the results reveals a gradual decrease in water absorption as the olive pomace content increases, reflecting greater connectivity within the pore network. The results obtained show that the capillary absorption test is a relevant method for evaluating the hydraulic behavior of olive pomace-reinforced soil-sand composites. This approach allows for an assessment of their suitability for use in sustainable construction applications while contributing to a better understanding of the relationships between formulation, porosity, and moisture transfer.

Keywords: *Raw earth, Bio-based composite, Capillary absorption, Porosity, Sustainable construction.*

I. Introduction

Earth-based building materials have attracted renewed interest in recent years as sustainable alternatives to conventional construction materials owing to their low environmental impact, local availability, low embodied energy, and excellent hygrothermal performance [1], [2]. Their use contributes to reducing greenhouse gas emissions while promoting the valorization of locally available resources within a circular economy framework. However, despite these advantages, earthen materials remain highly sensitive to moisture, which directly affects their physical, mechanical, thermal, and durability properties.

To improve the performance of earth-based materials while enhancing their sustainability, considerable research has focused on the incorporation of agricultural by-products as natural reinforcements. This approach not only promotes the valorization of agro-industrial waste but also improves several physical, mechanical, and thermal properties of earthen composites [3]. Among the various agricultural residues investigated, olive pomace has emerged as a particularly promising bio-based reinforcement because of its low density, abundant availability in olive-producing regions, renewable nature, and favorable thermal insulation properties [4], [5], [6]. Furthermore, its use represents an environmentally friendly solution for valorizing one of the major by-products generated by the olive oil industry.

The water behaviour of earthen materials is a key factor governing their suitability for construction applications. Moisture ingress directly influences dimensional stability, mechanical strength, thermal performance, and resistance to weathering. Among the various methods used to characterize water transport, the capillary water absorption test is widely recognized as one of the most appropriate techniques for evaluating the ability of porous materials to absorb and transport water through capillary action [7], [8], [9]. This

phenomenon mainly depends on pore size distribution, pore connectivity, total porosity, and the intrinsic characteristics of the material constituents.

The incorporation of olive pomace into a clay–sand matrix modifies the composite microstructure by increasing its porosity and altering the organization of the pore network. These microstructural changes influence moisture transfer mechanisms and consequently affect the hydraulic behaviour and durability of the material. Therefore, investigating capillary water absorption provides valuable insight into the influence of plant-based reinforcement on water transport mechanisms and the overall performance of the developed composites [10], [11].

The present study forms part of our ongoing research on the development and characterization of bio-based earthen composites reinforced with olive pomace [12]. The present contribution focuses on the hydraulic behaviour of these materials through the analysis of capillary water absorption. The objective is to evaluate the influence of different olive pomace incorporation rates on the capillary absorption behaviour of clay–sand composites and to establish correlations between this property and the main physical characteristics of the materials, including bulk density, porosity, and water-accessible pore structure. This work therefore completes the characterization of the developed composites and contributes to a comprehensive understanding of their hydro-mechanical and thermo-physical behaviour for sustainable construction applications.

II. Material and methods

This research focuses on the development of an eco-material composed of three main components: raw earth, sand, and olive pomace. This mixture aims to create energy-efficient bricks by utilizing local resources and agricultural waste. [12]

II.1 Raw materials

Here is a detailed description of these base materials:

II.1.1 Raw Earth

- Origin and nature: It was sourced locally in the Akbil region (Tizi Ouzou, Algeria). It is a reddish-ochre clay-loam soil.
- Role: It serves as the main matrix and natural binder of the composite due to its ability to form a cohesive structure after drying.

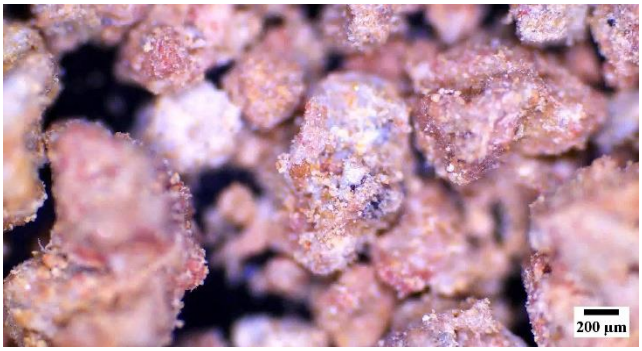

Figure 1. Raw earth Particles under Optical Microscope

II.1.2 Sand

- Origin: It comes from a local quarry and consists of light beige siliceous grains.
- Function: It is used as a granular stabilizing agent to reduce the plasticity of the soil mixture. Its function is to form a stable granular skeleton that improves mechanical strength and limits cracking and thermal shrinkage.

Figure 2. Sand Particles under Optical Microscope (200 µm)

II.1.3 Olive Pomace

- Origin: This is a solid byproduct of olive oil extraction, sourced from a local oil mill (Tizi Ouzou). It consists of crushed olive pits.
- Role: It serves as a lightweight, organic aggregate. Its incorporation aims to increase the material's porosity to improve thermal insulation (reducing thermal conductivity) and reduce the weight of the bricks.
- Preparation: Before use, it undergoes a cleaning process (washing with warm water) and is dried at 105°C to remove moisture.
- Properties: It is a porous, fibrous material with a low absolute density (1.15 g/cm³). It contains organic compounds such as lipids and esters.

Figure 3. Olive Pomace Particles under Optical Microscope (200 µm)

II.2 Raw materials characterization

Tests to Determine the Physical Properties of Base Materials

The physical characterization of the materials comprising the composites under study is a fundamental step in the development and performance evaluation of earth-matrix bricks reinforced with plant-based additives. These identification tests allow for the determination of the geotechnical and physical properties of raw earth, sand, and olive pomace in order to optimize the formulation of the mixtures and evaluate the influence of plant-based additives on the overall behavior of the composite. [12], [13].

In this study, several standardized tests were conducted in accordance with French AFNOR standards to ensure the reliability and reproducibility of the experimental results.

II.2.1 Characterization of Raw Earth and Sand

1- Particle Size Analysis

The particle size analysis was performed in accordance with standards NF P18-560 and NF P94-057 to determine the size distribution of the particles comprising the raw earth and sand. This characterization allows for the evaluation of the material's texture and the identification of the proportions of the various granular fractions (gravel, sand, silt, and clay).

The test involves passing the dry sample through a series of standard sieves of decreasing size to determine the percentages retained and passed by each sieve. The results obtained allow for the plotting of particle size distribution curves and the evaluation of the homogeneity of the materials studied.

For fine particles smaller than 80 µm, a sedimentation-based particle size analysis was also conducted in accordance with standard NF P94-057. This method is based on the settling velocity of particles in a fluid, in accordance with Stokes' law. It allows for the precise characterization of the silt and clay fractions present in the raw earth.

2- Sand Equivalent Test

The sand equivalent test was conducted in accordance with standard NF P18-598 to assess the cleanliness of the sand used and to quantify the presence of fine clay or silt particles that could influence the mechanical and hydraulic properties of the composite.

The principle of the test is based on the separation of sandy particles and fine particles in a flocculating solution. The ratio of the height of the settled sand to the total height of the suspension is used to calculate the sand equivalent value. A high value indicates clean sand with a low content of clay fines.

Figure 4. Sand Equivalent Test Apparatus.

3- Standard Proctor Test

The standard Proctor compaction test was conducted in accordance with standard NF P94-093 to determine the optimum moisture content and maximum dry density of the various mixtures under study.

Figure 5. Experimental Setup for the Standard Proctor Test.

The test involves compacting the material in a standard Mold in multiple layers using a specified compaction energy. For each moisture content, the corresponding dry density is calculated to plot the Proctor curve. The peak of this curve identifies:

- the optimum moisture content;

- the maximum dry density.

These parameters are essential for determining the optimal conditions for the application of the composites under study.

4- Determination of the absolute density of solid particles

The absolute density of the solid particles (ρs) in green clay and sand was determined using the water pycnometer method in accordance with standard NF P94-054.

This method involves measuring the volume occupied by a given mass of solid material in a pycnometer filled with water. The absolute density obtained allows for the characterization of the true density of the solid particles, independent of the voids present in the material.

This property is particularly relevant in calculations of porosity, compactness, and the formulation of composites.

5- Atterberg Limits

The Atterberg limits were determined in accordance with standard NF P94-051 to assess the plasticity of undisturbed soil and its behavior in relation to water.

The tests performed include:

- the liquid limit using the Casagrande pan;
- the plastic limit using the roller.

The liquid limit corresponds to the water content separating the liquid state from the plastic state, while the plastic limit represents the water content separating the plastic state from the solid state.

The difference between these two limits allows for the calculation of the plasticity index, an important parameter for assessing the soil's ability to be shaped and compacted.

Figure 6. Casagrande Apparatus for the Atterberg Limits Test.

II.2.2 Characterization of Olive Pomace

Olive pomace serves as the plant-based reinforcing material incorporated into the developed composites. Its physical characterization is necessary to assess its influence on the density, porosity, and thermal and mechanical properties of the developed materials.

1- Determination of the absolute density of olive pomace

The absolute density of the solid particles in olive pomace was determined using the graduated cylinder method.

The principle of this method is based on measuring the volume displaced after immersing a known quantity of olive pomace in a liquid. The density is then calculated from the ratio of the dry mass of the material to the displaced volume.

This characterization allows for the evaluation of the effect of plant-based additives on the lightweighting of the composite as well as on its porous structure.

II.3 The composite elaboration

The specimens were prepared by mixing raw earth, sand, water, and predetermined amounts of olive pomace (0%, 10%, 20%, and 30% by weight) until a homogeneous mixture was obtained. The resulting mixture was then placed into standardized moulds measuring 5 × 10 × 20 cm and compacted to ensure good cohesion and a uniform distribution of the constituents. For each of the four formulations, 5 brick specimens were manufactured, yielding a total of 20 specimens designated for testing to ensure statistical reliability. After demoulding, the specimens were placed on a flat surface and stored under ambient conditions, protected from direct sunlight. The drying process was carried out for 28 days to allow the gradual evaporation of water. During this period, the specimens were regularly turned over to promote uniform drying and minimize the formation of shrinkage-induced cracks. At the end of the curing period, the specimens were considered ready for physical characterization and capillary water absorption tests.

Table 1: The different dosages of composite components.

Formulation	(Raw earth + sand) %	Olive pomace %
00 %	100 %	00 %
10 %	90 %	10 %
20 %	80 %	20 %
30 %	70 %	30 %

Figure 7. The prepared composite brick specimens (5 x 10 x 20 cm)

II.4 The composite characterization

II.4.1 Optical Macroscopic Imaging Characterization

The prepared composites were characterized using an optical macroscope to examine their surface morphology and overall structural features. Macroscopic images were acquired in order to evaluate the distribution of olive pomace particles within the earth–sand matrix, identify the presence of pores, cracks, or other visible defects, and assess the homogeneity of the composite.

This technique provides a qualitative understanding of the influence of olive pomace incorporation on the material structure and complements the results obtained from physical and capillary absorption tests.

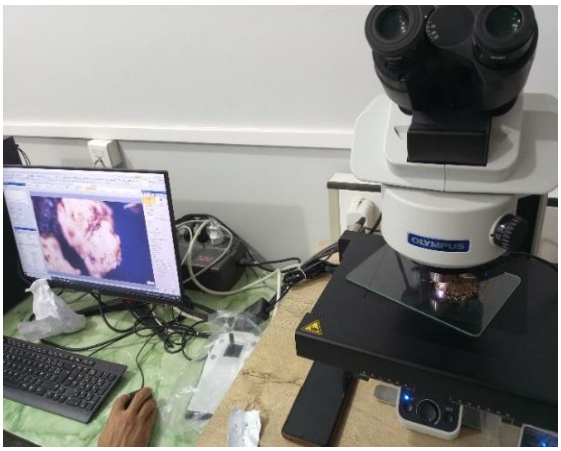

Figure 8. Optical Microscope Used for Sample Observation (OLYMPUS DP74)

Figure 9. Optical macroscopy image showing the microstructural features of the reference composite containing 0 wt.% olive pomace, observed at a scale of 200 µm.

The reference specimen (0 wt.% olive pomace), exhibits a relatively homogeneous surface morphology, characterized by a cohesive sand-clay matrix with a uniform distribution of constituents and minimal visible defects.

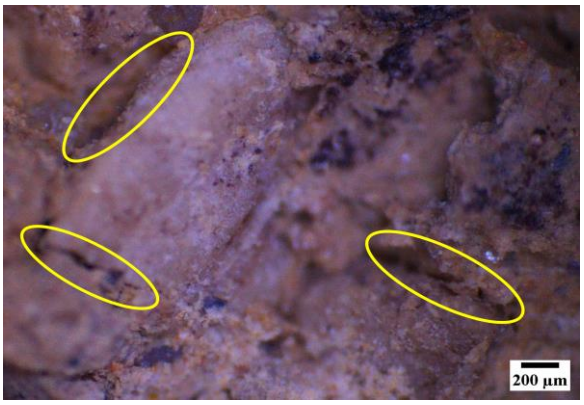

Figure 10. Earth–sand composite containing **10 wt.% olive pomace**, scale: 200 µm

Figure 11. Earth–sand composite containing **20 wt.% olive pomace**, scale: 200 µm

Upon the incorporation of 10 wt.% biomass (Figure 10), the microstructural arrangement begins to alter. The micrograph reveals the onset of minor interfacial defects, primarily manifested as microcracks along the matrix-filler interface.

As the olive pomace content increases to 20 wt.% (Figure 11), a progressive degradation of the interfacial zone is observed. This formulation displays a higher density and greater propagation depth of microcracks within the matrix–filler transition regions compared to the 10% olive pomace reinforced composite.

The 30 wt.% composite (Figure 12) exhibits the most pronounced structural disruption, characterized by significantly larger and more interconnected microcracks compared to the lower dosage formulations (10, 20 wt%).

Figure 12. Earth–sand composite containing **30 wt.% olive pomace**, scale: 200 µm

This progressive accumulation of interfacial microcracks and microstructural heterogeneity at higher biomass contents (20 wt.% and 30 wt.%) suggests a competing dual-mechanism governing the composite's hydraulic performance. While the olive pomace phase is anticipated to act as a physical barrier restricting water uptake, the localized development of matrix–filler defects may introduce preferential capillary pathways that mitigate further systematic reductions in absorption.

II.4.2 Characterization by capillary absorption testing

Capillary absorption tests were conducted in accordance with standard NF EN 772-11. To ensure rigorous repeatability and identical environmental exposure during testing, all four formulations (0%, 10%, 20%, and 30% olive pomace) were placed simultaneously into a single testing container for each test run. The testing was carried out in a temperature-controlled laboratory environment maintained at 20 ± 2°C and a relative humidity of 50 ± 5%.

Figure 13. Capillary absorption test in accordance with standard NF EN 772-11.

To guarantee experimental precision, the weight variations of the specimens during water absorption were recorded using a digital laboratory scale with an accuracy of ± 0.01 g. For the baseline physical characterizations, the water pycnometer used for solid particle density featured an accuracy of ± 0.001 g/cm³.

II.4.3 Statistical Analysis and Repeatability:

To evaluate the statistical significance of olive pomace content on the capillary water absorption coefficient, a one-way Analysis of Variance (ANOVA) was executed across the four experimental groups (0%, 10%, 20%, and 30%olive pomace) with 5 replicate specimens per formulation (total $N = 20$) [14]. Prior to running the parametric variance analysis, the underlying assumptions were verified: data normality within each group was assessed using the Shapiro-Wilk test [15], [16], and homogeneity of variances across groups was verified using Levene's test [17]. The overall magnitude of the effect of biomass addition was quantified using Eta-squared (η^2). To isolate specific localized differences between individual formulations, a post-hoc Tukey's Honestly Significant Difference (HSD) test was performed for pairwise mean comparisons [14]. All statistical computations were evaluated at a significance threshold of $\alpha = 0.05$using Python statistical libraries (scipy.stats and statsmodels). Visual representation of data dispersion and medians was achieved using box plots. Furthermore, it is well-established in statistical literature that the one-way ANOVA F-test is highly robust to minor violations of the normality assumption, particularly when sample sizes are equal across groups and variances are homogeneous [18].

III. Results and discussion

A. Results of tests to determine the physical properties of the base materials

Table 2: Physical properties summary for raw earth

Test properties	Parameters	Results
Particle Size Distribution (NF P 94-056) (NF P 94-057)	Sand	*48 %*
	Silt	*16 %*
	Clay	*36 %*
Proctor Test (NF P 94-093)	Optimum Moisture Content (OMC)	*24 %*
	Maximum Dry Density (Yd_{max})	*1,52 g/cm³*
Absolute density	Solid Particle Density	*2.6 g/cm³*
Dray Bulk density (NF P 94-059)	Bulk density (dry material)	*0.65 g/cm³*
Atterberg Limits (NF P94-051)	Liquid Limit (LL)	*68 %*
	Plastic Limit (PL)	*30.38 %*
	Plasticity Index (PI)	*37.62 %*
Soil Classification	Highly Plastic Clay Soil (*PI >35*)	

Properties:

Analyses show that it is highly plastic (Plasticity Index PI = 37.62%), which gives it excellent workability but requires the addition of sand to limit shrinkage during drying. Its chemical composition reveals the presence of hydrophilic clays such as **kaolinite** and **illite.**

Table 3: Physical properties summary for sand

Test properties	Parameters	Results
Particle Size Distribution (NF P 94-056)	Fine fraction (< 0.08 mm)	*0.75% (Very clean sand)*
	Grain distribution	From *0.2* to *1mm*
Sand equivalent (ES) (NF P 18-598)	ES Visual	*94.5%*
	ES Piston	*97.5%*
Proctor Test (NF P 94-093)	Optimum Moisture Content (w_{opt})	*8 %*
	Maximum Dry Density ($\rho_{d_{max}}$)	*1.98 g/cm3*
	Solid particle density (ρ_s)	*2.70 g/cm3*
Dry bulk density (NF P 94-059)	Bulk density (dry material) (ρ_d)	*1.54 /cm3*

Properties:

It is a very clean material (ES sand equivalent between 94% and 98%) and chemically inert, consisting mainly of quartz. Its absolute density is the highest of the three components (2.70 g/cm³).

B. Capillary Absorption results

The results of the capillary water absorption (water rise) test demonstrate that the incorporation of olive pomace significantly modifies the hygric behavior of earthen bricks.

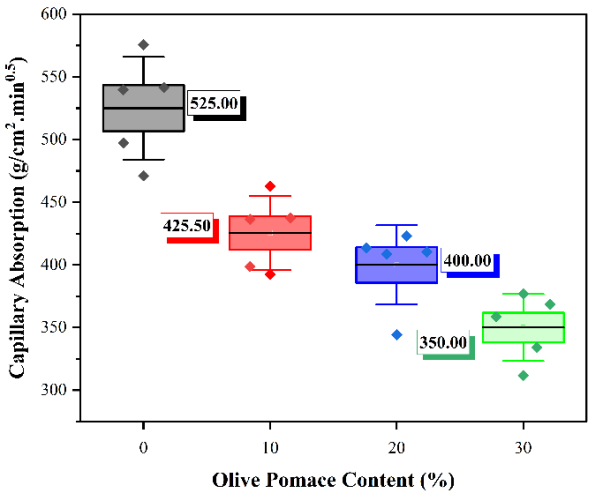

Figure 14. Box Plot for Capillary Absorption Test Results

To transition beyond a purely qualitative assessment of the composite's hygric behavior, a rigorous statistical evaluation was performed on the capillary absorption datasets derived from Figure 14. Prior to conducting the variance analysis, the formal assumptions of parametric testing were verified. Levene's test successfully confirmed the homogeneity of variances across all formulations ($p = 0.853$). While the Shapiro-Wilk test indicated normal data distributions for the 0%, 10%, and 30%formulations ($p > 0.05$), a slight deviation from normality was observed within the 20%formulation ($p = 0.014$). However, given that the study maintains strictly equal sample sizes ($n = 5$) and well-homogenized variances, the one-way ANOVA remains highly robust and mathematically valid for this dataset [18].

The one-way ANOVA revealed a highly significant effect of olive pomace content on the capillary absorption coefficient ($F(3,16) = 25.45, p < 0.001$). The calculated effect size was exceptionally substantial ($\eta^2 = 0.827$), indicating that approximately 82.7%of the entire observed variance in capillary water absorption is directly attributable to the dosage of olive pomace incorporated into the matrix.

To identify the exact thresholds where variations become statistically meaningful, a post-hoc Tukey's HSD test was executed. The results demonstrated that the control reference formulation (0%) exhibited a significantly higher capillary absorption compared to all bio-based modified formulations

($p \leq 0.001$), confirming that adding olive pomace structurally limits water uptake. This aligns with recent findings in bio-based composites where the incorporation of agricultural biomass alters the pore network and reduces capillary suction [19], [20]. When cross-examining the modified variations, no statistically significant difference was observed between the 10%and 20%contents ($p = 0.614$), nor between the 20%and 30%contents ($p = 0.112$). However, the 30%formulation exhibited a significantly lower water absorption coefficient than the 10%formulation ($p = 0.010$). This indicates a clear behavioral threshold: while an initial 10%addition forces an abrupt decline in capillary performance, further sequential steps yield diminishing statistical returns. This statistically positions the 10% to 20% envelope as highly efficient optimal configurations for minimizing moisture transmission without unnecessary material inflation, a phenomenon frequently observed when optimizing the dosage of organic waste in cementitious and earth-based matrices [5], [21], [22].

Experimental results

Measurements carried out on the bricks (5 × 10 × 20 cm) show an overall decreasing trend in water absorption with the addition of olive pomace:

- **Reference formulation (0% olive pomace):**
  It exhibits the highest absorption coefficient, reaching **525 g/cm²·min$^{0.5}$.**
- **Brick with 10% olive pomace:**
  The absorption drops to **425.5 g/cm²·min$^{0.5}$**. In terms of visible water rise height, this formulation shows the most significant reduction, with a decrease of **3.5 cm** compared to the reference sample.
- **Brick with 20% olive pomace:**
  The value continues to decrease, reaching **400 g/cm²·min$^{0.5}$**. However, the measured water rise height slightly increases to **8.0 cm**.
- **Brick with 30% olive pomace:**
  This formulation records the lowest absorption coefficient at **350 g/cm²·min$^{0.5}$.**

Phenomenon analysis

These variations can be explained by modifications in the internal structure of the material:

- **Pore network disruption:**
  The improvement in hygric behavior is attributed to the organic and fibrous nature of olive pomace. These fibers act as physical barriers that disrupt the continuity of the capillary pore network within the clay matrix, thereby slowing down the upward movement of water.
- **Heterogeneity at higher contents:**
  For 20% and 30% dosages, although the overall absorption coefficient decreases, a slight increase in water rise height is observed. This is explained by a more irregular distribution of olive pomace particles, which can locally create larger capillary pathways facilitating water migration.

IV. Conclusions

This study investigated the effect of olive pomace incorporation on the physical properties and capillary water absorption behavior of raw earth-sand composites for sustainable construction. The experimental results and subsequent statistical analysis lead to the following key conclusions:

- **Quantitative Reduction in Water Uptake:** The incorporation of olive pomace significantly improves the hydraulic resistance of the composites. The capillary absorption coefficient decreased progressively from 525 g/cm²·min$^{0.5}$ in the reference formulation (0%) to 350 g/cm²·min$^{0.5}$ in the 30 wt.% formulation.
- **Statistical Significance and Effect Size:** One-way ANOVA confirmed that olive pomace content has a highly significant effect on capillary behavior. Notably, the effect size indicates that 82.7% of the observed variance in water absorption is directly attributable to the dosage of biomass.
- **Identification of an Optimal Threshold:** Post-hoc Tukey HSD tests revealed a clear behavioral threshold. While the initial 10% addition causes an abrupt decline in absorption, sequential increases to 20% and 30% yield diminishing statistical returns. This positions the 10% to 20% envelope as the most efficient optimal configuration for minimizing moisture transmission.
- **Governing Mechanisms:** The reduction in capillary suction is primarily attributed to the disruption of the pore network, where organic fibers act as physical barriers. However, optical macroscopy (Figures 9-12) identified a competing dual-mechanism: at higher dosages (20% and 30%), the localized development of interfacial microcracks creates preferential capillary pathways that mitigate further systematic reductions in absorption.
- **Validation through Literature:** These findings align with recent studies on bio-based composites, confirming that agricultural by-products can effectively modify pore connectivity to enhance moisture durability.

Study Limitations and Future Work: While this study successfully characterizes hydraulic behavior, the increased porosity and interfacial defects at high replacement rates may impact other performance metrics. **Future work** will focus on evaluating the **long-term durability** to ensure these eco-bricks are structurally viable and energy-efficient for practical building applications.

A. Acknowledgment*:*
This research received no specific grant from any funding agency in the public, commercial, or not-for-profit sectors.

***List of symbols**:*

ρ_a	*Absolute density of solid particles*
ρ_{max}/ γ_{max}	*Maximum dry density*
OMC	*Optimum Moisture Content*
LL	*Liquid Limit*
PL	*Plastic Limit*
PI	*Plasticity Index*
ES	*Sand Equivalent*
$wt.\%$	*Weight Percentage*
F	*F-statistic (from One-way ANOVA)*
p	*Probability value*
η^2	*Eta-squared (measure of effect size)*
α	*Significance threshold*
N	*Total number of specimens*
n	*Sample size per group*
Q_1, Q_3	*First and third quartiles for box plot distribution*

References:

1. V. Mora-Ruiz, J. Soto-Paz, S. Attia, et C. Mejía-Parada. Sustainable Earthen Construction: A Meta-Analytical Review of Environmental, Mechanical, and Thermal Performance. Buildings vol. 15, n° 6, p. 918, janv. 2025, https://doi.org/0.3390/buildings15060918.

2. Y. G. Thyavihalli Girijappa, S. Mavinkere Rangappa, J. Parameswaranpillai, et S. Siengchin. Natural fibers as sustainable and renewable resource for development of eco-friendly composites: a comprehensive review. Frontiers in Materials vol. 6, p. 481024, 2019. https://doi.org/10.3389/fmats.2019.00226

3. M. Donner, I. Radić, Y. Erraach, et F. El Hadad-Gauthier. Implementation of circular business models for olive oil waste and by-product valorization. Resources vol. 11, n° 7, p. 68, 2022. https://doi.org/10.3390/resources11070068

4. K. Messara, S. Djadouf, et N. Chelouah, Properties and durability of compressed and stabilized earth blocks using excavated soil rich in limestone, Matériaux et Techniques vol. 112, n° 1, p. 107, 2024. https://doi.org/10.1051/mattech/2024017

5. I. Labaied, O. Douzane, M. Lajili, et G. Promis, From waste to value: olive pomace ash as a sustainable additive in clay-bricks. Journal of Material Cycles and Waste Management vol. 27, n° 5, p. 3307-3324, 2025. https://doi.org/doi: 10.1007/s10163-025-02292-7.

6. M. Bourbia, K. Kana, K. Mahmoudi, K. Amokrane, D. Louni, et N. Lardjane, Valorization of by-products from the olive oil extraction: evolution of chemical and spectroscopic characteristics during composting. Algerian Journal of Environmental Science and Technology vol. 2, n° 2, p. 20-25, 2016.

7. M. S. Camino, F. J. León, A. Llorente, et J. M. Olivar, Evaluation of the behavior of brick tile masonry and mortar due to capillary rise of moisture. Materiales de Construcción vol. 64, n° 314, p. e020-e020, 2014.

8. S. Guihéneuf, D. Rangeard, A. Perrot, T. Cusin, F. Collet, et S. Prétot. Effect of bio-stabilizers on capillary absorption and water vapour transfer into raw earth, Materials and Structures vol. 53, n° 6, p. 138, déc. 2020, https://doi.org/doi: 10.1617/s11527-020-01571-z.

9. R. Panagiotou et I. Ioannou. Capillary absorption into CEBs and 2-layer composite building materials comprising of natural stone and CEBs, in E3S Web of Conferences, EDP Sciences, 2023, p. 23006.

10. D. A. Samia, N. Chelouah, et A. Tahakourt. Study of the influence of agricultural waste on the porosity of clay brick, Materials Engineering vol. 22, n° 1, p. 16-24, 2015.

11. A. Jerónimo, M. Fernandes, et A. Briga-Sá. Experimental Study on the Potential Utilization of Olive Oil Production Wastes and By-Products as Building Materials, Sustainability vol. 16, n° 4, p. 1355, 2024. https://doi.org/10.3390/su16041355

12. K. Belmihoub, M. Salahi, M. Almansba, R. Ferhoum, M. Bencherif, et A. Boudedja, « Development of a composite material: raw earth, sand and olive pomace for use in sustainable construction, in *Book of Abstracts: International* Conference on Engineering Sciences for a Sustainable Environment (ICESSE'25), Tizi Ouzou, Algeria: Mouloud Mammeri University of Tizi-Ouzou, oct. 2025.

13. F. Khelouı, N. Boussaa, et N. Chelouah, Investigation of Wood Biomass Ash on the Thermal Behaviour of Compressed Earth Bricks. Eurasia Proceedings of Science, Technology, Engineering and Mathematics vol. 21, p. 412‑417, 2022. https://doi.org/10.55549/epstem.1226666

14. D. Montgomery et C. St, Design and Analysis of Experiments, 9th Edition. 2022.

15. G. D. Ahadi et N. N. L. E. Zain, Pemeriksaan Uji Kenormalan dengan Kolmogorov-Smirnov, Anderson-Darling dan Shapiro-Wilk. The Simulation Study of Normality Test Using Kolmogorov-Smirnov, Anderson-Darling, and Shapiro-Wilk. Eigen Mathematics Journal Vol 6, N° 1, p. 11-19, 2023. https://doi.org/10.29303/emj.v6i1.131

16. S. S. Shapiro et M. B. Wilk. An analysis of variance test for normality (complete samples). Biometrika vol. 52, n° 3-4, p. 591-611, 1965.

17. H. Levene. Robust Tests for Equality of Variances. In: Olkin, I., Ed., Contributions to Probability and Statistics, Stanford University Press, Palo Alto, 278-292, 1960.

18. G. V. Glass, P. D. Peckham, et J. R. Sanders. Consequences of Failure to Meet Assumptions Underlying the Fixed Effects Analyses of Variance and Covariance. Review of Educational Research vol. 42, n° 3, p. 237-288, 1972, https://doi.org/doi: 10.3102/00346543042003237.

19. B. Belaidi et al. Physical, Mechanical, and Durability Performance of Olive Pomace Ash in Eco-Friendly Mortars, Materials vol. 18, n° 11, p. 2667, 2025. https://doi.org/10.3390/ma18112667

20. D. Boukhelkhal, M. Guendouz, A. Bourdot, H. Cheriet, et K. Messaoudi, Elaboration of bio-based building materials made from recycled olive core, MRS Energy & Sustainability vol. 8, n° 2, 98-109, 2021, https://doi.org/doi:10.1557/s43581-021-00006-8.

21. K. Lila, S. Belaadi, R. Solimando, et F. R. Zirour. Valorisation of organic waste: Use of olive kernels and pomace for cement manufacture. Journal of Cleaner Production vol 277, 123703, 2020. https://doi.org/doi:10.1016/j.jclepro.2020.123703

22. M. Atigui et al. Enhanced Thermo-Physical Properties of Gypsum Composites Using Olive Pomace Waste Reinforcement. Revue des Composites et des Materiaux Avances vol. 34, n° 1, 67-75, 2024. https://doi.org/doi: 10.18280/rcma.340109